

Photometric rotation periods for 107 M dwarfs from the APACHE survey

P. Giacobbe,^{1*} M. Benedetto,² M. Damasso,¹ A. Sozzetti,¹ J.M. Christille,²
 M.G. Lattanzi,¹ P. Calcidese,² A. Carbognani,⁵ D. Barbato,^{4,1} M. Pinamonti,¹ E. Poggio
 A. F. Lanza,³ A. Bernagozzi,² D. Cenadelli,² L. Lanteri,¹ E. Bertolini²

¹*Astrophysical Observatory of Torino, INAF, Strada Osservatorio 20, Pino Torinese (To) 10025, Italy*

²*Astronomical Observatory of the Autonomous Region of the Aosta Valley, Frazione Lignan 39, Nus (Ao), 11020, Italy*

³*Astrophysical Observatory of Catania, INAF, Via S. Sofia 78, Catania, 95123, Italy*

⁴*Department of Physics, University of Torino, Via Pietro Giuria 1, I-10125 Torino, Italy*

⁵*Astrophysical and Space Science Observatory of Bologna, INAF, Via Gobetti 93/3, Bologna, 40129, Italy*

Accepted XXX. Received YYY; in original form ZZZ

ABSTRACT

We present rotation period measurements for 107 M dwarfs in the mass range $0.15 - 0.70M_{\odot}$ observed within the context of the APACHE photometric survey. We measure rotation periods in the range 0.5–190 days, with the distribution peaking at ~ 30 days. We revise the stellar masses and radii for our sample of rotators by exploiting the *Gaia* DR2 data. For $\sim 20\%$ of the sample, we compare the photometric rotation periods with those derived from different spectroscopic indicators, finding good correspondence in most cases. We compare our rotation periods distribution to the one obtained by the *Kepler* survey in the same mass range, and to that derived by the MEarth survey for stars in the mass range $0.07 - 0.25M_{\odot}$. The APACHE and *Kepler* periods distributions are in good agreement, confirming the reliability of our results, while the APACHE distribution is consistent with the MEarth result only for the older/slow rotators, and in the overlapping mass range of the two surveys. Combining the APACHE/*Kepler* distribution with the MEarth distribution, we highlight that the rotation period increases with decreasing stellar mass, in agreement with previous work. Our findings also suggest that the spin-down time scale, from fast to slow rotators, changes crossing the fully convective limit at $\approx 0.3M_{\odot}$ for M dwarfs. The catalogue of 107 rotating M dwarfs presented here is particularly timely, as the stars are prime targets for the potential identification of transiting small planets with TESS and amenable to high-precision mass determination and further atmospheric characterization measurements.

Key words: stars: low-mass – stars: rotation – stars: statistics – techniques: photometric

1 INTRODUCTION

The efficacy of the two techniques (transit photometry and Doppler spectroscopy) that have enabled the detection of the overwhelming majority of exoplanets known to-date (~ 4000 , see e.g. <https://exoplanetarchive.ipac.caltech.edu/> and <http://exoplanet.eu/>) can be fundamentally hampered by insufficient understanding of photometric and spectroscopic signals that are stellar and not planetary in nature. For instance, stellar magnetic activity cycles

with typical timescales of several years of duration can be a serious concern when claiming detection of long-period planets in radial-velocity (RV) time-series (e.g., [Carolo et al. 2014](#); [Endl et al. 2016](#)). In such cases, the ability to discriminate the true nature of the signals crucially depends on the availability of spectroscopic proxies for stellar activity and/or photometric monitoring. When it comes to M dwarf type planet hosts, the stellar temperate zone, within which the signals of potentially habitable planets can today be readily identified in principle (e.g., [Anglada-Escudé et al. 2016a](#); [Dittmann et al. 2017](#); [Suárez Mascareño et al. 2017a](#); [Astudillo-Defru et al.](#)

* E-mail: paolo.giacobbe@inaf.it

2017b; Bonfils et al. 2018; Zechmeister et al. 2019), corresponds to orbital periods typically in the range of tens of days (e.g., Kopparapu et al. 2013, 2014; Kopparapu 2018). However, these timescales can coincide with those of stellar rotation periods of low-mass stars in the middle of their main-sequence lifetime (e.g., Barnes 2007; McQuillan et al. 2013; Vanderburg et al. 2016; Newton et al. 2016; Suárez Mascareño et al. 2018). Without a detailed understanding of stellar activity-induced effects in RVs to supporting spectroscopic and photometric information, ambiguities in the interpretation of RV signals with periods corresponding to habitable zone distances might be long-lasting (e.g., Robertson et al. 2014; Anglada-Escudé & Tuomi 2015; Robertson et al. 2015; Anglada-Escudé et al. 2016b). Even in the case of transiting systems, for which the periodicity of the planetary signal can be unambiguously identified via transit photometry, the proximity between orbital and insufficiently well characterized rotation periods can undermine our ability to determine dynamical masses with high statistical confidence (e.g., Cloutier et al. 2017; Damasso et al. 2018, 2019).

The fraction of low-mass M dwarfs harbouring temperate super Earth-type planets is likely to be high (e.g., Bonfils et al. 2013; Dressing & Charbonneau 2015; Hardegree-Ullman et al. 2019). This is one of the reasons why they figure prominently as main targets of important ground-based RV surveys (e.g., Affer et al. 2016; Astudillo-Defru et al. 2017c; Luque et al. 2018; Hobson et al. 2019). For the Transiting Exoplanet Survey Satellite (TESS; Ricker et al. 2014), launched in 2018 April, small habitable-zone planets around M dwarfs constitute a particularly relevant sample (e.g., Sullivan et al. 2015; Barclay et al. 2018; Ballard 2019; Kaltenegger et al. 2019), as the combination of small telescope aperture and satellite’s observing strategy translate in a low mission sensitivity to orbital periods longer than a few tens of days (except near the ecliptic poles) and to planets with radii $\lesssim 2 R_{\oplus}$ around solar-type primaries. Measurements of photometric rotation periods for M dwarfs with TESS-detected small-size transit candidates would be of paramount importance to gauge the effects of spots in the analysis of the transit events and to help disentangling planetary RV signals from those related to stellar magnetic activity (e.g., Haywood et al. 2014; Vanderburg et al. 2016; Dittmann et al. 2017; Damasso et al. 2018). However, rotation periods of a few tens of days or longer will not be typically accessible to TESS (at least during its nominal mission lifetime), due to its less than a month duration of the observing windows. Follow-up efforts can thus take advantage from the availability of additional data that can aid in the characterization of the detected systems.

In this paper we present rotation periods for 107 nearby, early- to mid-M dwarfs in the northern hemisphere using photometric time-series with a multi-year time baseline gathered within the context of the APACHE (A Pathway towards the CHaracterization of Habitable Earths) photometric transit search project (Sozzetti et al. 2013). With TESS now beginning to survey the northern hemisphere, the study presented here is particularly timely, as all of the bright M dwarfs in the sample objective of this work are prime targets for the potential identification of transiting small planets amenable to high-precision mass determination and

further atmospheric characterization measurements (TESS mission Level 1 Requirement). Our sample of rotation periods can also be used to further our understanding of important issues of stellar astrophysics pertaining to partly and fully convective stars, such as differences in rotational evolution (e.g., Gilhool et al. 2018, and references therein) and the age-rotation-activity relation (e.g., Wright et al. 2018; González-Álvarez et al. 2019).

The paper is organized as follows: in Sec. 2 we introduce the APACHE photometric survey; in Sec. 3 we describe our input catalogue; in Sec. 4 we present our results; in Sec. 5 we compare our findings with the literature from the spectroscopic survey HADES and the photometric surveys *Kepler* and MEarth; in Sec. 6 we summarize our findings and we discuss some points of interest related to the exoplanet research and the M dwarfs stellar physics.

2 THE APACHE SURVEY

2.1 Infrastructure

APACHE employs an array of five 40-cm telescopes hosted on a single platform with a roll-off enclosure, located at the Astronomical Observatory of the Aosta Valley (OAVdA), in the western Italian Alps, at 1650 meters above the sea level. The site characterization study was presented in Damasso et al. (2010), while a feasibility study of the APACHE project was presented in Giacobbe et al. (2012). The telescope array is composed of five identical Carbon Truss 40-cm f/8.4 Ritchey-Chrétien telescopes, with a GM2000 10-MICRON mount and equipped with a FLI Pro-line PL1001E-2 CCD Camera and Johnson-Cousins V & I filters. The pixel scale is $1.5''/pixel$, yielding a field-of-view (FOV) of $21' \times 21'$. The open source observatory manager RTS2 (Kubánek 2010) was the choice for the high-level software control of the five-telescope system, including dynamic scheduling of the observations (Christille et al. 2013).

2.2 Observational strategy

As APACHE is a targeted survey, its sampling strategy differs from that of wide-field transit surveys (e.g., HATNet; Bakos 2018, Super-WASP; Pollacco et al. 2006), and it more closely resembles that of other experiments, which adopted the ‘one target per field’ approach (e.g., MEarth and MEarth-South; Nutzman & Charbonneau 2008). The optimal observing strategy should maximize the number of targets observed per night while preserving a time sampling good enough to detect transit events due to short-period planets. Exploiting the data collected within the pilot study (Giacobbe et al. 2012), a series of detailed simulations with different temporal sampling and number of exposures was performed in order to choose the optimal observing strategy. In particular, we tested intervals of 10 through 50 minutes between two sets of consecutive pointings of the telescope on the same target, and 1 to 5 consecutive exposures for each pointing. Eventually, we adopted for APACHE an observing strategy consisting of 3 consecutive exposures every 20 minutes. In this way, during a typical night of observation, each telescope observes ~ 12 fields, where the greater part of them contain only a single target M dwarf. Each target

is observed for the whole time available during the night with airmass below 2. Exposure times are selected to yield a signal to noise ratio (SNR) for the target star > 200 while avoiding detector saturation.

2.3 Data reduction and differential photometry analysis pipeline

Data reduction and analysis were carried out using a dedicated software package written in IDL, which utilizes free libraries from the Astronomy User’s Library and external routines in FORTRAN and C++. It is organized into modules:

- image calibrations (dark, bias and flat-fielding subtraction);
- image alignment (via astrometric solution) and photometric processing (aperture photometry);
- differential photometry and trend filtering.

While image calibration and alignment implement standard procedures for which it is not necessary to provide lengthy descriptions, the extraction of the light curve in the third module of the pipeline deserves more attention, so we describe it here in more details. This component of the pipeline performs those operations that are necessary to correct, to a high degree of reliability, for systematic effects that cause the degradation of the photometric quality and consequently of the transit detection efficiency. This is a fundamental step of the pipeline because it provides the starting point, but also the validation benchmark, for more sophisticated filtering procedures.

We start by applying a straightforward differential photometry technique: for each frame i , we use the average magnitude of n reference stars $M_{ref}(i)$ according to the equation

$$M_{ref}(i) = \frac{\sum_{k=0}^n M_k(i)}{n} \quad (1)$$

where the M_k time-series are zero-averaged. The normalized magnitude of the target $M_{target}(i)$ is then subtracted from $M_{ref}(i)$, obtaining the difference $\Delta M(i)$

$$\Delta M(i) = M_{ref}(i) - M_{target}(i) \quad (2)$$

corrected for all the common systematics. In this process there are two key points: i) we need the most accurate estimate of the instrumental magnitude $M_{ref}(i)$ and $M_{target}(i)$ and ii) we need the best set of reference stars (e.g. excluding variable stars or stars affected by peculiar systematic errors like bad pixels). For the point i), we have implemented a multi-aperture photometric processing. We settled on 12 apertures, typically ranging from two to four times the average full width at half-maximum (FWHM) of the point spread function. While for the point ii), we first take care of picking up reference objects on a CCD subframe, avoiding the chip edges, affected by vignetting which is not fully corrected for during flat-fielding. Secondly, in order to choose the appropriate set of references for the target we use a method based on the [Burke et al. \(2006\)](#) prescription. This method selects the subset of reference stars which minimizes the RMS of the differential light curve of the target and it is then applied to all 12 apertures in order to choose the optimal one, on the basis of a minimum-RMS prescription

for the target light curve. The target and the reference stars use the same selected aperture.

Although the standard photometric procedure performs very well on nightly basis, there are some residual systematic effects after this processing. As described before, APACHE uses German Equatorial Mounts, which necessitate effectively rotating the telescope through 180° relative to the sky when crossing the meridian. Thus, each set of reference stars (not the target that is always in the center of the detector) falls on two areas of the CCD, one for negative and one for positive hour angle. In this situation, flat fielding errors manifest themselves as different base-line magnitudes on each side of the meridian. Following the discussion in [Berta et al. \(2012\)](#), dealing with the same problem in MEarth, we call this effect “mount-flip”. Secondly, we observe correlations between the measured differential magnitudes of the target M dwarfs and weather parameters, specifically the sky brightness (which depends in turn from the presence of clouds/cirri and the lunar phase). Thirdly, we observe a correlation between the amplitudes of the systematics that affect the targets and the amplitudes of the (same) systematics that affect the reference stars. Probably, the last two correlations are produced by a mismatch, in particular in spectral type, between the target star and the comparison stars. In other words, each target over a period of years shares a linear combination of the systematics of the field. Considering this, we can’t guarantee with the “standard” procedure the stability of the systems at mmag level over a period of many years.

Furthermore, we investigate the effect of the precipitable water vapour, a systematic effect with a significant impact on the photometric performance of other M dwarfs surveys, such as MEarth ([Berta et al. 2012](#)). We follow closely the approach proposed by [Berta et al. \(2012\)](#), looking for a “common mode” across our M dwarfs sample, without finding a clear correlation with it and, consequently, with no need to build a common mode function. This is likely due to two reasons: 1) we observe with the I -band filter, a photometric band less affected by telluric absorption with respect to the redder custom-made MEarth filter; 2) our sample is mainly constituted by early-type M dwarfs with a color index more similar to that of field stars.

In this context, a reliable filtering algorithm is mandatory to reach the photon noise level over the full observation period. Our best solution adapts the Trend Filtering Algorithm (TFA, [Kovács et al. 2005](#)) to our purpose and peculiarity. The principal goal of our trend filtering algorithm is to create a so called “filter function” representing the systematic effects influencing the target light curve. This “filter function” can be considered as a data-driven model where there is no a priori knowledge of the systematics that we want to filter and it is built directly from the field stars light curve.

The first step is to collect the reference stars light curves in a matrix X . To build X we consider the full set of reference stars excluding only those stars clearly variable, on the basis of the deviation between each star’s RMS light curve derived by the standard photometry and the theoretical single point uncertainty derived by Eq. 7. While for the differential photometry we generally select a set of few reference stars, our trend filtering algorithm requires as many reference stars as possible, in order to be sure to include all the systematics of the field. Furthermore, as mentioned be-

fore, there are a set of systematics poorly sampled by the reference stars but strongly present in the final differential light curves. We insert them directly inside the X matrix. To solve the “mount-flip” we create a single-row matrix that models the orientation of the mount (we put a value of 0 if the mount was oriented to East, 1 otherwise) and we add it as a new row of the X matrix. Similarly, we create a model representing the “global” sky background (inserting frame by frame its measured mean value on the field) and we add it as a new row of the X matrix as explained before. The sky background for each of the stars in the FOV is computed using an annulus around the source with dimensions generally between four and seven times the aperture for the sources’ photometry.

Then we create a model of the filtered light curve $A(i)$

$$A(i) = \sum_{j=0}^M \frac{X_j(i)}{M} \quad (3)$$

where M is the total number of reference objects plus “mount-flip” and sky background. The filter function $F(i)$ is now defined according with the equation

$$F(i) = \sum_{j=0}^M c^j X^j(i) \quad (4)$$

To determine the c^j coefficient we minimize the expression D

$$D = \sum_{i=0}^N [Y(i) - A(i) - F(i)]^2 \quad (5)$$

via Singular Value Decomposition (SVD), where Y is the target light curve vector and N is the number of observations. The filtered light curve $\tilde{Y}(i)$ is finally obtained by

$$\tilde{Y}(i) = Y(i) - F(i) \quad (6)$$

We consider the RMS of the light curves as a proxy of the impact of this kind of systematic correction over the data quality. In Fig. 1 we show the distribution of the single point uncertainty σ_t (black solid line), the RMS precision of the “standard” differential photometry (red dotted line) and the RMS precision of the light curves detrended with our trend filtering algorithm (blue dashed lines). While the RMS precision of the “standard” differential photometry is heavily affected by systematic effects, with our filtering we are able to approach the theoretical distribution with a clear improvement of the data quality.

Sometimes this kind of correction could be too aggressive and it might contribute to suppress the signal amplitude. As described in Sec. 4.1, after the steps just mentioned we use the Generalized Lomb-Scargles (GLS) algorithm (Zechmeister & Kürster 2009) to find a sinusoidal signal, with periodicity and phase. If the signal has a False Alarm Probability (FAP) $\leq 1\%$, we use the Foreman-Mackey et al. (2015) approach to preserve and rebuild it. With the GLS results we create a rotation model with amplitude equal to 1, then we add it to the X matrix as a new row. Applying TFA again with the new X matrix we treat the signal as a systematic, we correct it and we obtain its amplitude. We therefore have a completely corrected light curve, the signal period, phase and amplitude. Once rebuilt, the rotation

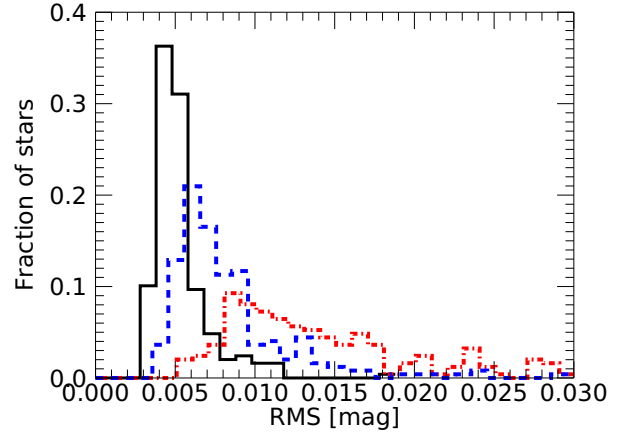


Figure 1. Fraction of stars as a function of RMS for the APACHE sample. The black solid line shows the distribution of the single point uncertainty σ_t , the red dotted line shows the distribution of the RMS precision of the “standard” differential photometry, the blue dashed line shows the distribution of the RMS precision of the light curves detrended with our trend filtering algorithm.

signal is added to the reduced light curve. A similar approach, with the goal to filter out the systematics without affecting the signal, was developed by Berta et al. (2012). The main, but substantial difference is that the algorithm by Berta et al. (2012) performs the filtering plus signal search after the standard differential photometry (that is a sort of pre-whitening) while our method, based on the framework established by Foreman-Mackey et al. (2015), performs the filtering plus signal search together with the differential photometry. Nevertheless, the idea to describe the systematics poorly sampled by the reference stars using some analytical functions closely follow Berta et al. (2012). The combination of the two techniques ultimately allows for a more thorough treatment of systematics.

3 THE INPUT CATALOGUE

3.1 Initial target selection

The APACHE Input Catalogue was built as a sub-list of the all-sky sample of 8889 bright (magnitude $J < 10$) low-mass stars in Lépine & Gaidos (2011). After checking the visibility constraints from OAVdA (at least 3 hours per night with altitude $\geq 30^\circ$ and over a period of at least 2 months), the number of potentially good (at least 5 stars with V magnitude within 1 magnitude from the target) comparison stars in the telescopes’ field-of-view and the absence of relevant blended objects, we selected ~ 3000 targets composing our final Input Catalogue. Then, we devised a ranking system to identify targets with higher priorities taking into account the survey scientific goals (in particular the detection of small size planets) and architecture. The ranking was principally based on the best observability during the year and on V magnitude of the targets, considering it as a key point for the RV followup. Then, we consider the number of the *Gaia* transits based on accurate representation of

Gaia's scanning law, in order to prioritize those in areas of the sky with higher numbers of *Gaia* astrometric measurements. Furthermore, we cross-correlate with approximately two dozen catalogs, searching for additional and more precise information than that included in Lépine & Gaidos (2011), such as *i*) a better determination of the spectral class, to avoid spectral types different from M dwarfs; *ii*) measurements of projected rotational velocity $V\sin i$, to favour slow rotators in that they are more suitable for precise RV follow-up; *iii*) level of chromospheric activity and X-ray emission, to flag active targets which are not optimal to search for low-mass planets with the RV technique. Given the huge impact for the exoplanet research of the synergies between spectroscopic and photometric measurements, we override our prioritization for all that targets selected for high-precision RV monitoring with the HARPS-N spectrograph on the Telescopio Nazionale Galileo (TNG) within the Global Architecture of Planetary Systems (GAPS) (e.g. Desidera et al. 2014; Benatti et al. 2016) and HARPS-N red Dwarf Exoplanet Survey (HADES) collaborations (e.g. Affer et al. 2016; Perger et al. 2017; Affer et al. 2019).

3.2 Observations logbook and performances

The data considered in this paper are the results of five year of observation between 9th July 2012 and 9th July 2017. This period corresponds to the nominal duration of the survey. From the APACHE observations database, we select a sub-sample of 247 M dwarfs with more than 200 data points taken on at least 10 observation nights and spanning at least 30 days. We obtained a typical per measurement theoretical single point uncertainty of ~ 0.005 mag (see the bottom right panel in Fig. 2) and a median long-term RMS precision on the light curves of ~ 0.007 mag (see Sec. 2.3 for further details and Fig. 1).

The theoretical single point uncertainty σ_t , in magnitudes, is defined by

$$\sigma_t = \frac{2.5}{\ln 10} \times \frac{\sqrt{N_{star} + N_{sky} + \sigma_{scint}^2}}{N_{star}} \quad (7)$$

where N_{star} is the number of photons from the source, N_{sky} is the number of photons from the sky background for the photometric aperture that includes read and dark noise and σ_{scint} is the scintillation noise (Young 1967).

Fig. 2 summarizes the overall properties of the 247 selected M dwarfs. In Tab. A1 we present the observational properties for all the targets¹, while our results are presented in Tab. A2 for our candidate rotators. Overall, 81% of the targets have more than 500 observations and they were observed for more than one observing season, while $\approx 7\%$ of the targets, considered as schedule fillers, have a low number of observations (≤ 150). Although our strategy was mainly driven by the transit search and it was not optimized for the rotation period detection, we note that the data quality and the phase coverage are very suitable to look for rotational period. We quantitatively discuss this point in Sec. 4.

3.3 Revised stellar properties from *Gaia* DR2

For the aim of this work, it is important to assign a reliable mass and radius estimation of our M dwarf sample. We estimate them using the FORTRAN evolutionary track interpolator² based on the Yale-Potsdam stellar isochrones (Spada et al. 2013, 2017), taking as inputs the effective temperature T_{eff} , metallicity $[Fe/H]$ and luminosity L_* . The uncertainties on stellar masses and radii are derived with a Monte Carlo approach, running again the interpolator in a $0.25 M_\odot$ neighborhood centered on the M_\odot obtained from the first run of the interpolator and using input values of T_{eff} , $[Fe/H]$ and L_\odot randomly drawn from a Gaussian distribution having standard distribution equal to each parameter's archive uncertainty. From this new run of the evolutionary track interpolator we therefore obtain distributions of M_* and R_* , the standard deviations of which are then used as the $1-\sigma$ uncertainties of stellar masses and radii. For each star in the sample, we retrieve from the *Gaia* DR2 archive values for T_{eff} and parallax π ; the latter is then used to compute stellar luminosity L_\odot . Having no high-resolution near-infrared spectra available that would enable a reliable chemical characterization of the stars, we fix the input metallicities at $[Fe/H] = 0$ dex; this choice is a reasonable assumption for the analysed stellar types and is further supported by a recent study on a similar sample of M dwarfs by Newton et al. (2016) for which near-infrared spectra estimate an average iron abundance comparable to 0 dex. Of the 247 stars in our sample, 27 are not found in the *Gaia* DR2 archive and 3 have no *Gaia* estimate of T_{eff} ; for these stars the use of the Yale-Potsdam interpolator was therefore not possible. In Fig. 3 we show the mass distribution of our M dwarfs sample on which the period search was performed with the mass distribution of the subsample with measured rotation overplotted (dash-dotted red line). We perform the two-sided Kolmogorov-Smirnov (K-S) statistic test to evaluate the associated probability p_{K-S} that the two mass distributions are drawn from the same distribution function. We obtain $p_{K-S} = 0.9999$, with therefore a high likelihood of the two mass distributions having been drawn from the same cumulative distribution function. We conclude that there is not a clear bias in the period detection (see Sec. 4.1) with respect to the mass.

Since the uncertainty over the mass estimation ($\leq 10\%$) heavily benefits from the *Gaia* DR2 data, we re-derive, as described above, the values of mass and radius of the M dwarf sample with measured rotation from Irwin et al. (2011). We select this sample despite the fact that it is a sub-sample of more recent works like Newton et al. (2016) and Newton et al. (2018) because there are many similarities with the statistical properties of the APACHE sample, e.g. number of targets observed, number of photometric points per target, phase coverage, photometric single point uncertainties. Furthermore, the most recent works do not drastically revise the statistics presented in the first paper, so we can use this sub-sample as a proxy of them. In Fig. 4 we present the fractional differences between the masses of the Irwin et al. (2011) sample as derived by the authors and the masses as derived in this work as function of stellar mass.

¹ the light curves of all the 247 stars are available upon request by e-mailing the author

² available at <http://www.astro.yale.edu/demarque/yystar.html> and last updated on May 2018

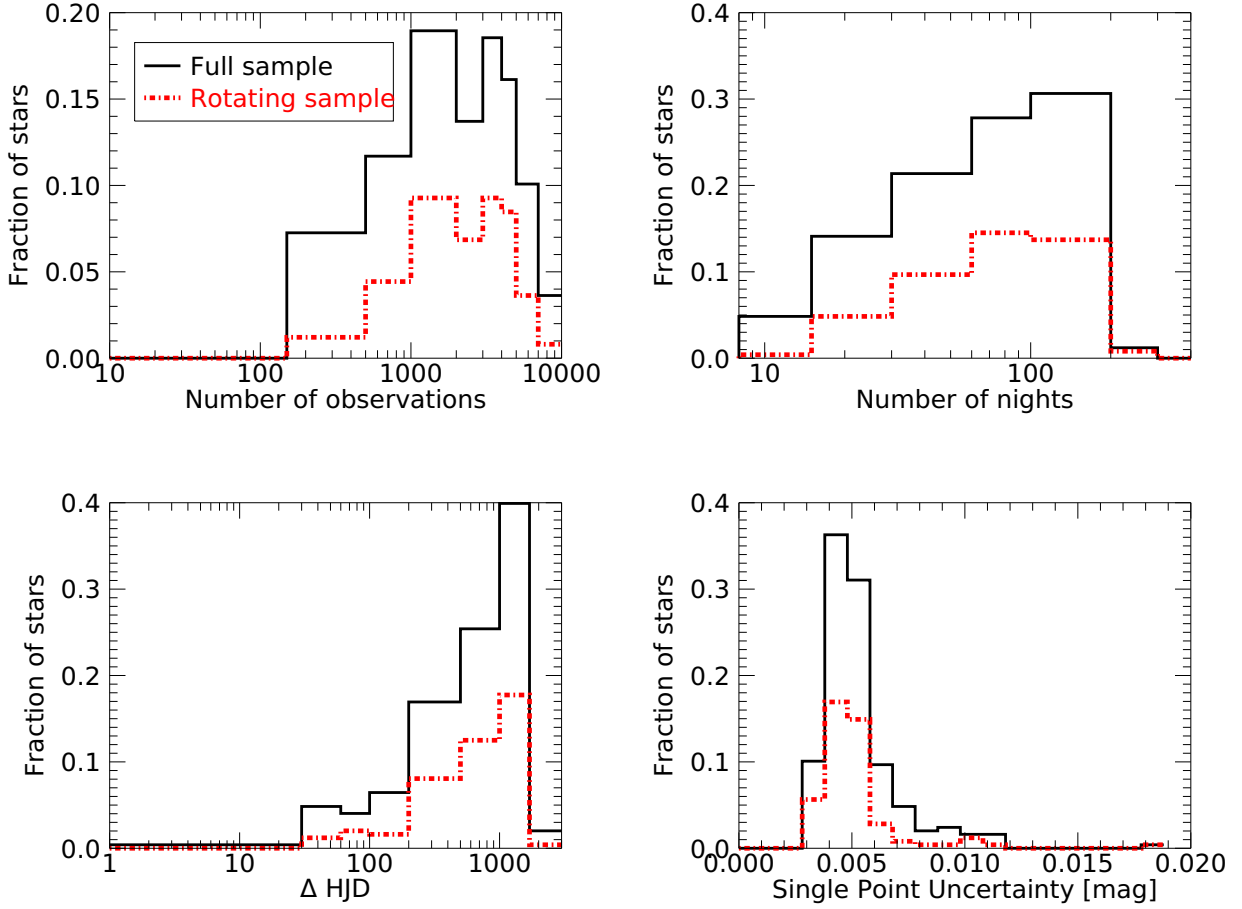


Figure 2. Top left: fraction of stars as a function of the number of observations. Top right: fraction of stars as a function of the observation nights. Bottom left: fraction of stars as a function of the time span between the first and the last observation. Bottom right: fraction of stars as a function of the mean theoretical single point uncertainty. The black solid line represents the full sample of 247 M dwarfs considered for the rotation period research while the dash dotted red line represents the sample of 107 M dwarfs with detected rotational modulation.

It shows differences up to 60 % and a slight systematic shift of our mass estimations towards bigger values for the less massive stars.

4 RESULTS

4.1 Period detection

As described in Sec. 2.3, the output of our pipeline is a light curve where the vast majority of the systematic effects are properly accounted for. So, at the first order, we can assume that the variance of the final light curve is composed only by photon noise, correlated and uncorrelated stellar jitter and, if present, the stellar signals as the modulation induced by the presence of spots. Therefore, we searched for sinusoidal-like modulation in the light curves without any other filters by using the complete dataset binned at 30 minutes. The bin width was selected in order to increase the SNR and to weaken the short time scale correlated noise while preserving a time sampling good enough to detect rotation periods < 1 days. We used the GLS to calculate the frequency pe-

riodograms sampled on a uniform grid in frequency corresponding to the period interval between 0.1 and 500 days. To estimate the significance of the detection, we performed a bootstrap analysis (with replacement) using 10000 randomly permuted data-sets derived from the original binned photometric data. We select all the objects with $FAP \leq 1\%$, while the final sample of periodic variables was done on the basis of a visual inspection. One hundred eight light curves passed this selection, where the other 140 light curves were consistent with no detectable variation, had excessive residual systematics, or had insufficient phase coverage to determine the true period.

Here we note again that, in order to avoid the underestimation of the signal amplitude due to the de-trending algorithm, we correct for the systematics and fit the sinusoidal signal simultaneously, as described in Sec. 2.3, for all the targets in the final rotating sample.

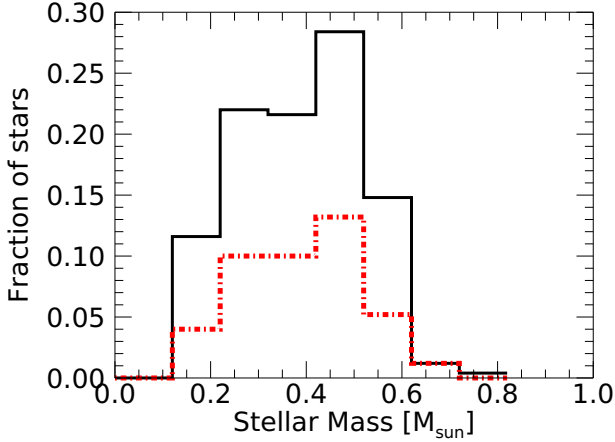


Figure 3. Fraction of stars as a function of stellar mass for the APACHE sample. The black solid line shows the distribution of the sample of 247 M dwarfs stars on which the period search was performed while the dash-dotted red line represents the distribution of the subsample with detected rotational modulation.

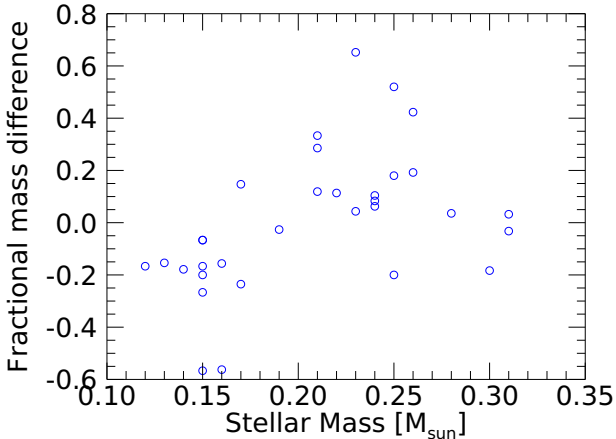


Figure 4. Fractional mass difference between the masses derived by Irwin et al. (2011) and the masses as derived in this work as a function of stellar mass.

4.2 Rotation period distribution

The rotation period distribution of the sample of 107 M dwarfs with detected rotational modulation is shown in the left panel of Fig. 5, while the results are presented in Table A2. The distribution’s peak lies at ~ 30 days with a minimum rotation period of 0.52 days and a maximum of 191.82 days. Despite our sensitivity decreases at longer periods, in this range it is substantially unbiased, as shown in Sec. 4.5. Fig. 6 shows rotation period plotted as a function of stellar mass, where the filled symbols indicate our kinematic population assignments from Sec. 4.3. Looking at Fig. 6 and considering the upper periods envelope, the periods are observed to increase with decreasing mass.

While the thin disk sample spans the full range of pe-

riods and includes entirely the rapidly rotating objects, the thick disk sample is constituted by only slowly rotating stars. The situation is similar to the thin disk sample for the stars with an intermediate kinematics classification, with no objects in the ultra fast ($P < 5$ days) rotating clump. We discuss this point in the next Sections, but given the mean old age of the thick disk, this indicates that the older objects in the sample are rotating more slowly. As shown in Fig. 7, our findings are in agreement with the Irwin et al. (2011) MEarth sample revised in mass and kinematics by this work. In any case, the mean ages of the thin and thick disks only provide a weak metrics to understand the rotational evolution of the M dwarfs.

4.3 Kinematics characterization (as a proxy of the mean age of the sample)

As discussed in the previous Section, the rotational period distribution is a function of mass and age. The age assignment for the field M dwarf stars is not trivial. A tentative solution is to use the available kinematic information to infer a rough estimate of the stellar age. For our sample, we consider the *Gaia* DR2 astrometric parameters (positions, parallaxes and proper motions) and line-of-sight velocities, when available. When the line-of-sight velocity is not available from *Gaia* DR2, we consider the reference value from SIMBAD³ and reference therein. The distance to the stars is then calculated by naively inverting *Gaia* DR2 parallaxes. All the stars in our sample have $\varpi/\sigma_\varpi > 10$, indicating that the obtained distances are not prone to the biases associated with large fractional parallax error (Bailer-Jones 2015). We derive 3D positions and velocities in Galactocentric cylindrical coordinates $R, \phi, Z, V_R, V_\phi, V_Z$ where R is the distance from the Galactic center, ϕ is the Galactic azimuth (defined as positive in the direction of Galactic rotation), Z is the height from the Galactic plane and V_R, V_ϕ, V_Z are the velocities components along the coordinates described above. We assume for the Sun a distance to the Galactic center of $R_\odot = 8.122$ kpc (Gravity Collaboration et al. 2018), a vertical height above the Galactic midplane $Z_\odot = 0.027$ kpc (Chen et al. 2001) and a Galactic azimuth of the Sun $\phi_\odot = 0$. We assume for the Sun a velocity $(V_{R,\odot}, V_{\phi,\odot}, V_{Z,\odot}) = (-12.9, 245.6, 7.78)$ km/s (Drimmel & Poggio 2018). Kinematic information can be used to estimate the mean stellar age of the sample by statistically assigning our targets to the Galactic thin disk or thick disk/halo populations. In particular, the Galactic thick disk is characterized by high-velocity dispersions, a unique chemistry and remarkably old age. For the stars of our sample, we therefore calculate the total velocity with respect to the Local Standard of Rest (LSR) V_{TOT} as

$$V_{TOT} = \sqrt{V_R^2 + (V_\phi - V_{LSR})^2 + V_Z^2} \quad (8)$$

with $V_{LSR} = 233.4$ km/s (Drimmel & Poggio 2018; Schönrich et al. 2010). We identify thick disk star candidates as the ones with $80 \text{ km/s} < V_{TOT} < 180 \text{ km/s}$ (following Nissen 2004), whereas thin disk stars are expected to have $V_{TOT} < 60 \text{ km/s}$ (Nissen 2004). We define a mid disk population as all those stars with the intermediate 60 km/s

³ (<http://simbad.u-strasbg.fr/simbad/>)

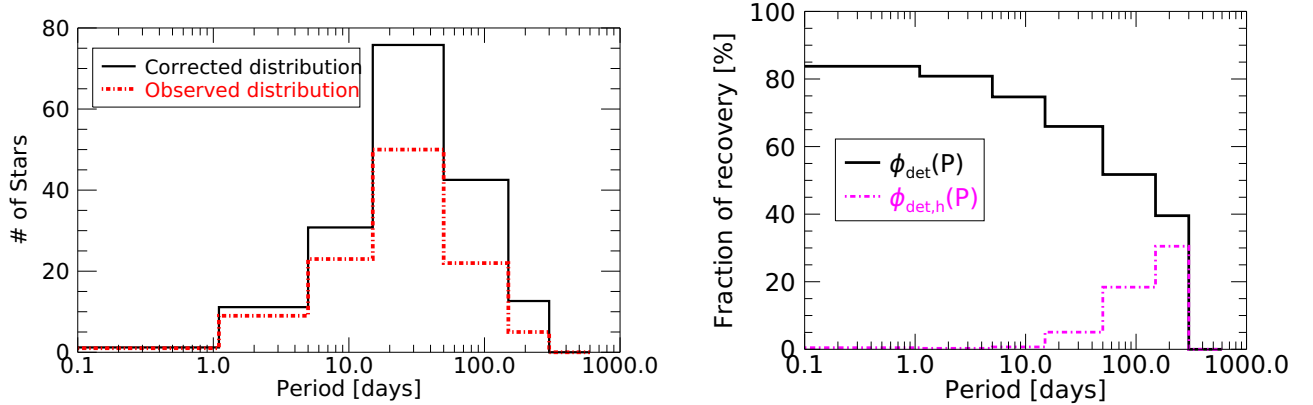


Figure 5. Left panel: the solid black line represents the number of stars as a function of rotation period for the APACHE sample while the dash dotted red line represents the number of stars corrected for the detection efficiency as a function of rotation period. Right panel: the solid black line represents the detection efficiency $\phi_{det}(P)$ derived from the simulations as a function of rotation period while the dashed magenta line represents the harmonic contamination $\phi_{det,h}(P)$ derived from the simulation as a function of rotation period.

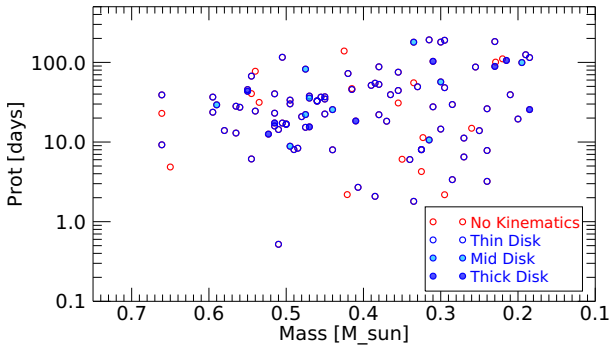


Figure 6. Rotation period as a function of stellar mass for the APACHE sample. The red circles represent the stars with no kinematics characterization. The blue circles represent the targets with kinematics characterization, where the unfilled circles are the stars more likely belonging to the thin disk, and the filled ones belonging to the thick disk. The filled light blue circles have an intermediate kinematics between the two populations.

$< V_{TOR} < 80$ km/s kinematic. According to this method, our sample with measured rotation contains $\sim 80\%$ of thin disk stars, $\sim 10\%$ of mid disk stars, while $\sim 10\%$ of stars are thick disk stars. This is in agreement with the stellar number density distribution of the Milky Way from the Sloan Digital Sky Survey (SDSS) in the Solar neighborhood (Jurić et al. 2008). In Fig. 8 we show the Toomre diagram (e.g. Gaia Collaboration et al. 2018) of the APACHE sample in red and the Newton et al. (2016) sample in blue, using the velocity vector components published in Newton et al. (2016) for the MEarth sample. The filled symbols are the stars associated with mid/thick disk. In Newton et al. (2016) they found that $14\% \pm 3\%$ of “grade A” rotators likely belonged to the thick disk, a number becoming $7\% \pm 3\%$ considering the grade A + B rotators. No stars with detected rotation were found to belong to the halo populations. On this basis, we can consider the two samples as equivalent in

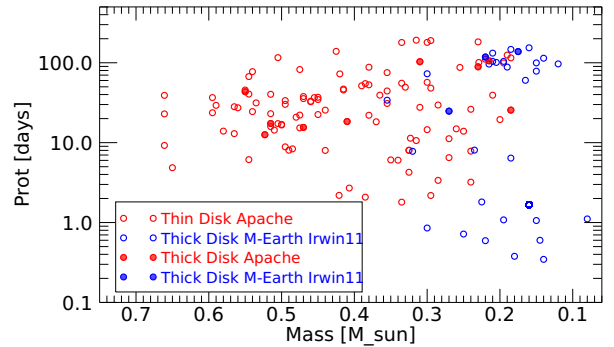


Figure 7. Rotation period as a function of stellar mass. The red circles represent the stars from the APACHE sample while the blue circles represent the stars from the M-Earth Irwin et al. (2011) sample. The filled circles are the stars more likely belonging to the thick disk. For clarity we do not show the stars with the intermediate kinematic but the two samples are in agreement.

terms of kinematic populations, and, consequently, equivalent in terms of age distribution, according to the kinematic population/age relation presented in Newton et al. (2016) and discussed here. This is not an unexpected result, considering that the samples are selected in the solar neighborhood.

Finally, we assign to the thin disk stars a mean age of ~ 3 Gyr while to the thick disk stars a mean age of ~ 10 Gyr (e.g., Feltzing & Bensby (2008)).

4.3.1 The age-velocity dispersion relationship

As well observed in the open clusters at different ages (e.g., Herbst et al. 2002, Hartman et al. 2009, Prosser et al. 1995), the low-mass main-sequence stars spin down with time. Therefore, as highlighted in Sec.4.2, it is expected that slow rotators (the upper envelope in the rotation period-mass relation) are older than their more rapidly rotating

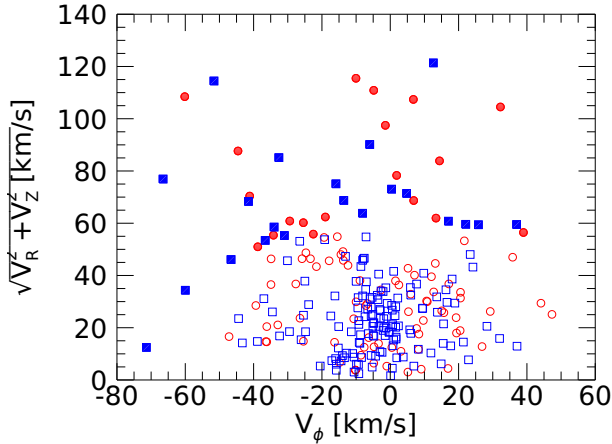


Figure 8. $\sqrt{V_R^2 + V_Z^2}$ as a function of V_ϕ for the APACHE sample with measured rotation (red circles) and the MEarth-N (Newton et al. 2016) sample (blue square). The filled symbols are the stars associated with mid/thick disk.

counterparts. While in clusters there are robust method to constrain the ages and therefore the rotational evolution of low mass stars over a grid of young ages, there are no reliable methods to determine the ages of isolated field M dwarfs.

Looking at the age-velocity dispersion relation in the solar neighbourhood (e.g. Yu & Liu 2018, Aumer & Binney 2009), we investigate the signature of an age-rotation relation in the distribution of total space velocities, as defined in Eq.8, as a function of photometric rotation period. Fig.9 shows the total space velocity as a function of measured photometric rotation period, where the blue circles are the stars from the APACHE sample while the blue circles represent the stars from the MEarth-N Newton et al. (2016) sample. We use the Spearman rank correlation coefficient for total space velocity V_{TOT} and rotation period which is 0.22 for APACHE sample while the Spearman rank correlation coefficient published by Newton et al. (2016) for the full sample of MEarth late M dwarfs is 0.18, a value in good agreement with that derived for the APACHE sample. Assuming that the velocity dispersion increases with age, as expected for an older stellar population that has been dynamically heated, the star’s ages are increasing with rotation period.

In order to adopt the age-velocity relation as published in Yu & Liu (2018) or Aumer & Binney (2009), we need to estimate the dispersion of the V_Z velocity component, σ_{V_Z} . We determine the σ_{V_Z} that underlies our data closely following the Bayesian approach described in Newton et al. (2016). Following their discussion, we divide our sample into bins in period, $P < 1$ day, $1 < P < 10$ days, $10 < P < 70$ days, and $P > 70$ days. In Tab. 1 we summarize our findings, compared to the results by Newton et al. (2016). We use the age-velocity relation as published in Aumer & Binney (2009) in order to compare our results with the MEarth survey. In any case, the considerations presented here, based on a relatively small sample and a large intrinsic error, are not affected by the used relation. It is useful here to remember that the APACHE and MEarth samples do not cover the same mass range but rather can be considered as comple-

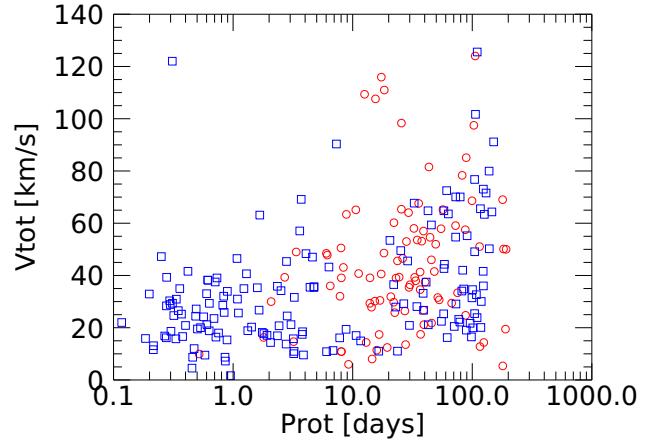


Figure 9. Total space velocity V_{tot} as a function of rotation periods. The red circles represent the stars from the APACHE sample while the blue squares represent the stars from the MEarth Newton et al. (2016) sample.

Table 1. Velocity dispersion σ_{V_Z} and estimated ages for M dwarfs with detected rotation periods from APACHE and MEarth-N. The values reported here for the MEarth surveys are published in Newton et al. (2016), Table 6

Period Bin (Days)	N stars #	Mean P (days)	σ_{V_Z} (km/s)	Est. Age Gyr
APACHE				
$0.1 < P < 1$	1	0.52
$1 < P < 10$	16	6.14	$19.9^{+3.8}_{-10.2}$...
$10 < P < 70$	58	29.63	$14.6^{+2.3}_{-2.3}$	$3.3^{+0.6}_{-0.6}$
$P > 70$	17	122.49	$20.1^{+3.4}_{-10.5}$...
MEarth-N				
$0.1 < P < 1$	39	0.5	$6.0^{+1.8}_{-1.0}$	$0.5^{+0.4}_{-0.2}$
$1 < P < 10$	23	2.9	$7.4^{+1.8}_{-1.8}$	$0.7^{+0.3}_{-0.3}$
$10 < P < 70$	10	28.3	$6.5^{+1.6}_{-1.8}$...
$P > 70$	14	102.4	$16.7^{+5.3}_{-4.5}$	$4.5^{+3.9}_{-2.3}$

mentary across the M dwarf mass range. We exploit this in order to track the M dwarfs’ rotational evolution path and relative time scales as a function of the stellar mass.

For the APACHE sample the only period’s bin well sampled is in the range $10 < P < 70$. For it, we adopt a mean age of 3.3 ± 0.6 Gyr. In this bin, our mean age is comparable with the mean age in the $P > 70$ range for the MEarth sample. This is a further proof of how the upper envelope of the period-mass relation (see Sec. 5.2 and Sec. 5.3 for further details) is a function of mass with the late mature M dwarfs rotating slower in comparison with the early mature M dwarfs. In the other bins our results are not robust enough to assign a mean age.

4.4 Amplitude of variability

The amplitude of the periodic photometric modulation associated to the stellar rotation depends to the contrast between the spotted and unspotted stellar photosphere and the longitudinal inhomogeneity in the distribution of spots. Since the starspots are related with the stellar activity, which is in

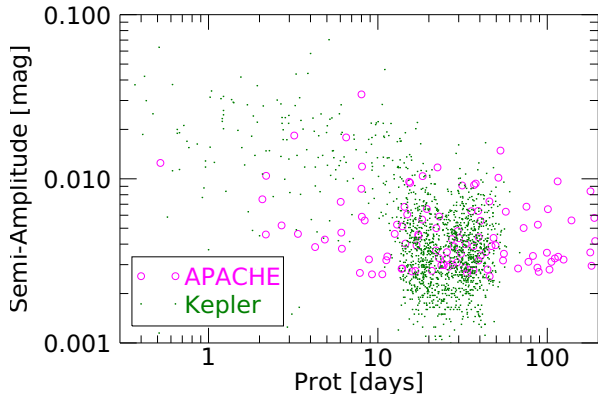


Figure 10. Semi-amplitude of the signal as a function of rotation period. The red circles represent the stars from the APACHE sample while the green dots represent the stars from the *Kepler* McQuillan et al. (2013) sample.

turn related to stellar age, the stellar rotation and the variation of the magnetic fields, we investigate the correlation between rotation period, mass and photometric amplitude of the signals. Fig. 10 shows the semi-amplitude of the signal as a function of rotation period. There is not a clear correlation between the amplitude of the signals and the rotation period. This is confirmed by McQuillan et al. (2013) for M dwarfs in the *Kepler* sample (we discuss more in details the comparison between APACHE and *Kepler* in Sec. 5.2) although they observed a bigger dispersion of the amplitude in the fast rotators. It is important to note that the amplitude of the periodic signals of the *Kepler* stars could be reduced by the MAP pipeline used to reduce the data analysed by McQuillan et al. (2013), in particular for periods longer than 30-40 days (see Fig. 6 in Gilliland et al. (2015)).

In any case, considering that the amplitude of the flux modulation depends also on the inclination of the star spin axis, we do not exclude that the amplitudes distribution may be dominated by a sort of geometrical effect. Furthermore, we do not model any evolution or non-sinusoidal behavior. In these cases the “global” semi-amplitude is suppressed relative to the peak-to-peak amplitude that was instead measured by McQuillan et al. (2013).

4.5 Simulation

In order to evaluate our sensitivity in period and amplitude, simulations were performed using the following method: for each target we inject 10000 sinusoids with periods from 0.1 to 200 days following a uniform distribution in frequencies. For each period, we randomly extract the reference phase in the range between 0 and 1. A fixed semi-amplitude was adopted in our simulations, 0.002 mag, corresponding to the minimum amplitude of our rotation candidates (see Fig. 13 or Tab. A2). We inject the synthetic signals into the 140 light curves with no period detection, as described in the previous section, while we made synthetic light curves for the other targets. For each synthetic light curve we randomly add noise generated according to a Gaussian distribution

with sigma equal to the mean single point uncertainty derived from the real data. Each simulated light curve was processed exactly in the same way of the real data, as described in Sec. 4.1. We have a detection if the retrieved period differs from the true injected period by $\leq 1\%$. We define the detection efficiency $\phi_{det}(P)$ as the relative number of periods that are detected by GLS with respect to the total number of injected periods. Although we did not consider as a detection the multiple and the sub-multiple periods of the true injected period, we can use them to investigate the possible contamination by the harmonics in our period distribution. We have a detection of an harmonic or sub-harmonic (up to the fourth harmonic or subharmonic) if the retrieved period differs from the corresponding harmonic or sub-harmonic of the injected period by less than 1%. We define the harmonic contamination $\phi_{det,h}(P)$ as the relative number of harmonics that are detected by GLS with respect to the total number of injected periods.

Our estimation of detection efficiencies allows us to investigate the presence or not of bias into our period distributions due to the single point uncertainty, the time sampling and the phase coverage of the data. We correct the measured period distribution with $\phi_{det}(P)$: due to the phase coverage no clear bias is evident. The corrected period distribution is shown in the right panel of Fig. 5. We highlight that this “corrected” distribution does not account for bias in masses or activity levels but only for the survey sensitivity and, summarizing, it is useful to quantitatively address the quality of our data and the position of the distribution peak under the hypothesis of the initial sample selection.

The result in terms of recovery rate, as well the harmonics’ contamination, is summarized in the left panel of Fig. 5. The statistics indicate very good period recovery, 80%-60%, for the bins between 0.1-100 days while it drops in longest-period bin, where the completeness reduces to $\sim 40\%$. On the other side, the harmonics’ contamination is 0% for the bins between 0.1-15 days while it grows up in the longest-period bin, where the contamination increases to $\sim 30\%$. This is expected due to the limited survey duration and the intrinsic difficulties to take into account annual trends due to the instrumental instability. It is interesting to note that the 98% of the harmonics’ contamination is due to the half or the double of the true injected period.

For each target, we evaluate a mean detection efficiency Φ_{det} and a mean harmonics’ contamination $\Phi_{det,h}$ in the whole range 0.1 to 200 days and we report these values in Tab. A1.

Φ_{det} and $\Phi_{det,h}$ could be useful, in certain cases, to try to break down the degeneracy between the true period and its harmonics (see Sec. 5.1 for some examples) due to the phase coverage and time sampling. Furthermore, it could be considered as a further check on the reliability of the periods published in this work.

5 THE APACHE PERIOD DISTRIBUTION IN A WIDE CONTEXT

5.1 Spectroscopic rotation periods

As part of a joint exoplanet-hunt effort, as discussed in Sec. 3.1, 44 of the APACHE targets were also monitored

Table 2. Rotational periods of the 23 Apache targets in common with Suárez Mascareño et al. (2018). In the $P_{rot,H}$ sources column we denote the methods to derive the rotation periods from the spectroscopic data.

Name	$P_{rot,A}$ (days)	$P_{rot,H}$ (days)	$P_{rot,H}$ sources
J06147+4727	27.320	23.0 ± 4.0	estimated
J07316+6201W	67.240	15.0 ± 3.0	estimated
J09133+6852	19.450	10.4 ± 0.1	Act ind
J01013+6121	75.350	34.7 ± 0.1	Act ind, RV
J12350+0949	18.260	55.0 ± 5.5	Act ind
J17158+1900	14.540	37.0 ± 13.0	Act ind
J17166+0803	45.690	85.0 ± 15.0	estimated
J18596+0759	43.400	25.0 ± 5.0	estimated
J21129+3107E	20.830	18.0 ± 4.0	estimated
J21185+3014	8.060	7.80 ± 0.2	Act ind, RV
J12194+2822	22.910	23.2 ± 0.1	Act ind, RV
J16254+5418	87.969	77.8 ± 5.5	Act ind, RV
J14294+1531	12.570	43.5 ± 1.5	Act ind
J18353+4544	33.620	34.5 ± 4.7	Act ind
J17160+1103	32.990	33.6 ± 3.6	Act ind, RV
J11000+2249	179.920	58.0 ± 10.	estimated
J11511+3516	36.980	40.0 ± 8.0	estimated
J14257+2337W	17.360	36.6 ± 0.1	Act ind
GJ3649	30.150	15.0 ± 3.0	estimated
J02565+5526S	103.100	51.2 ± 4.4	Act ind
J03437+1640	22.490	25.0 ± 5.0	estimated
J04086+3338	8.360	32.4 ± 1.6	Act ind, RV
J04587+5056	7.990	25.0 ± 5.0	estimated

spectroscopically by the HADES program. The HADES targets were investigated for the presence of rotation signals in the spectroscopic data by Suárez Mascareño et al. (2018), who studied the Ca II H and K and H α chromospheric activity indicators, the RV series, and the parameters of the cross correlation function. We detected significant periodic variability in the APACHE photometry for 23 of these 44 stars, while the other 21 lightcurves did not pass the quality checks described in Sec. 4.1. For 13 stars over these 23, Suárez Mascareño et al. (2018) were able to measure the rotation periods from the spectroscopic activity indexes (Ca II H&K and/or H α) or RV time series, while for the other 10 the rotation period was estimated from activity-rotation relationships and their calculated values of $\log R'_{HK}$. The definition of $\log R'_{HK}$ was extended for application on M dwarfs spectra, following a procedure very similar to the one used by Suárez Mascareño et al. (2016). We summarize the properties of this subsample in Tab. 2.

Fig. 11 shows the comparison between the APACHE and HADES rotation periods. We can see that for most stars there is a good correspondence between either the two rotation periods or one rotation period and the first harmonic of the other. It is worth noticing that only for five targets there is a larger discrepancy: two estimated HADES rotation periods on the lower-right corner of the plot appear to be largely underestimated with respect to the measured photometric periods, with one close to the second harmonic of $P_{rot,A}$; on the upper-left side of the plot, instead, there are three HADES measured periods which appear to be overestimated, and close to three times the photometric period. There is no apparent reason for these discrepancy with respect of the rest of the sample, as these stars do not appear

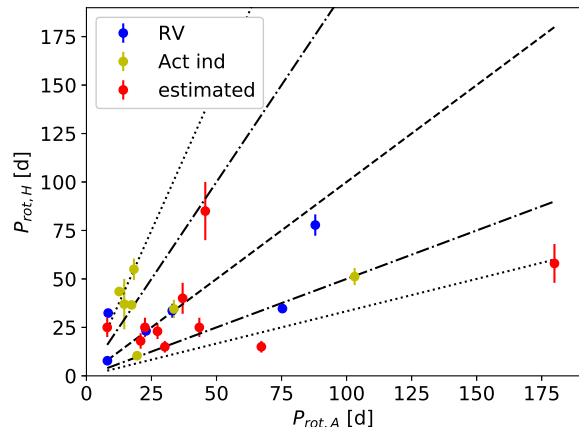


Figure 11. Comparison between the photometrically-derived rotation periods from APACHE $P_{rot,A}$ in days and the spectroscopically-derived ones from HADES $P_{rot,H}$ in days. The blue dots represent the targets with measured HADES rotation periods from RV time series, the yellow dots represent the targets with spectroscopic rotation periods derived from the activity index time series while the red dots represent the targets with spectroscopic rotation periods estimated from activity-rotation relationships. The dashed black line represents the $P_{rot,H} = P_{rot,A}$, the dash-dotted lines represent where one rotation period is either double or one half of the other while the dotted lines represent where one rotation period is either triple or one third of the other.

to be either particularly active or quiet, and follow the general distribution of stellar parameters.

However, the photometric stellar signal at the rotation period is caused by stellar spots. It is therefore important to note the existence of a “pathological” spot distribution (e.g two identical active regions longitudes spaced by 180°) which can lead to doubling of the frequency, causing to misestimate the true rotation period of the star (Collier Cameron et al. 2009). Furthermore, the period estimations from activity-rotation relationships are affected by an uncertainty by a factor of 2-3 at a given level of activity (e.g, Suárez Mascareño et al. (2015); Astudillo-Defru et al. (2017a)). The level of activity, in fact, changes due to activity cycles and the evolution of active regions. One should follow a star for a time comparable with its activity cycle to be sure that the average level of activity is correctly determined. For this reason and from the nature of the activity-rotation relationships, which is precisely an empirical relationship and not a direct measurement, we suggest that these disagreements are not a cause of concern, despite all the other uncertainties described in this Section.

Looking at the particular cases, the periods from activity-rotation relationships that are not on the 1:1 line do not seem to be randomly distributed in the diagram, as expected in the case of a wrong estimation. There are two cases, J17166+0803 and J04587+5056, where we found double or triple periods of the photometric period. Looking at the simulations, there is a low probability to have an harmonic contamination for these two cases. Taking into account that the probability to have an harmonic contamination is drastically lower than the probability to have a sub-harmonic contamination, a similar conclusions could be

done for the rest of the targets that do not lie on the 1:1 line. We highlight here that our detection efficiency and harmonic contamination are calculated under the assumption that the signal induced by the rotation could be modelled with a sinusoid. We are not able to assess here the impact of this assumption on the detection efficiency.

Double or triple periods of the photometric period are found for different stars in the case of measurements based on chromospheric indices. For these objects, we have a low probability harmonics contamination from our simulation. Taking into account that they are quite long periods, between 30 and 50 days, they could be associated with the timescale of evolution of the active regions that could dominate over the rotational modulation signal.

If we especially consider the periods obtained with the RVs, they are in agreement with the photometric ones in four cases out of six. In one case, J01013+6121, the period from the RV is close to the first harmonic and this is observed in certain cases, even in the Sun as a star (Mortier & Collier Cameron 2017). Looking at a $\Phi_{det} = 61\%$ and a $\Phi_{det,H} = 0\%$ (see Sec. 4.5 for the details), there are no reasons to suppose that the APACHE period estimation for this target is an harmonic of the true period. The only anomalous case, J04086+3338, is when the RV measurement is close to four times the photometric period. In particular, we estimate a rotation period of 8.36 days with a semi amplitude of 0.0056 mag, while the measured HADES rotation period is 32.4 ± 1.6 days. From our simulation, we have a $\Phi_{det} = 21\%$ and a $\Phi_{det,H} = 17\%$, that denotes a quite low detection efficiency for periods longer than 15 days and a consequent contamination of the true period by the harmonics. In this case, we probably miss the true period due to the low temporal sampling in the APACHE photometry. Generally speaking, such a type of discrepancies could be also explained as an effect of the "noise" necessarily present in the RV series, since the star is quite active and rotates in less than 10 days (according to photometry).

Focusing on the HADES targets with detected planetary systems which were present in the final sample of APACHE rotation periods, GJ 3998 (Affer et al. 2016) and GJ 625 (Suárez Mascareño et al. 2017b), we see a good agreement between the published spectroscopic rotation periods and the photometric values presented in this work. Moreover, we notice that for GJ 685 we do not present here any rotation period since the stellar rotation signal is very weak in the APACHE photometry (Pinamonti et al. 2019), and it did not pass the quality checks of the present analysis.

Our comparison with the rotation periods derived by the spectroscopy suggests that a contamination between the true period and its harmonics could be possible. The only way to break down this degeneracy is to acquire more data, both spectroscopic and photometric. In any case, although the true periods estimation is indeed what one aims for, detection of the harmonics of the true period is still a useful piece of information. For the vast majority of the objects presented here the rotation period estimate based on APACHE photometry is the only measurement available. These data therefore could represent an important reference point for further investigations, such as those aiming at spectroscopic follow-up of small-radius transiting planets below the APACHE sensitivity but that might be detected by space-based photometric programs (e.g., TESS, CHEOPS).

5.2 Comparison to *Kepler* photometry

The large sample of rotating M dwarfs from the *Kepler* survey published in McQuillan et al. (2013) is ideal to compare with the APACHE sample. McQuillan et al. (2013) measured the rotation periods of 1570 M dwarfs (of the 2483 stars examined) in the mass range $0.3-0.55 M_{\odot}$, corresponding to the mass range of APACHE. As shown in Fig. 14, the periods distributions from *Kepler* and APACHE are in good agreement. We perform another K-S test to evaluate the associated probability that the two distributions are drawn from the same distribution function. We obtain $p_{K-S} = 0.883$, indicating that *Kepler* and APACHE distributions are consistent with the samples being drawn from the same cumulative distribution function. As shown in Fig. 14, if we consider a denser binning in order to reproduce the Fig 9 of McQuillan et al. (2013), we note that the two distributions are different aside two details: i) while the *Kepler* period distribution is clearly bimodal, with peaks at ~ 19 and ~ 33 day, the APACHE period distribution does not show it clearly. McQuillan et al. (2013) supposed that this bimodal behaviour hints at two distinct waves of star formation, a hypothesis that could not be true for our sample. Furthermore, as shown in Sec. 5.1, we often observe degeneracy between multiples, sub-multiples and the true periods. Taking into account the smaller dimension of our sample combined with this effect, we are probably not able to resolve this bimodality, if present; ii) McQuillan et al. (2013) did not detect rotation periods longer than 70 days in any of their objects, although they searched as long as 155 days. Probably, this is mostly due to the initial selection of the *Kepler* sample which virtually does not include fully convective stars and therefore should not have periods longer than 70 days according to the observed mass-period relation. On the other hand, we can not exclude that this discrepancy could be also explained as a combination of at least three effects: 1) it is possible that *Kepler*'s systematics, particularly due to the rotation of the satellite every ~ 90 days, affect the recovery of longer rotation periods. Furthermore, Gilliland et al. (2015) shows that the sensitivity for periods $\geq 15-20$ days is lower than expected; 2) as shown in Sec. 5.1, the degeneracy between multiples and submultiples of the true period could also affect the statistic on the longer periods; 3) McQuillan et al. (2013) estimated masses from the *Kepler* Input Catalogue (KIC) effective temperatures without precise parallaxes. Since parallaxes and T_{eff} are not available in DR2 for the majority of the *Kepler* M dwarfs, it is not possible to derive the masses with the same method described in 3.3. Therefore, there may be an offset between the two mass scales, as also shown in Berger et al. (2018). Since the rotation periods become longer for older stars, as shown in Newton et al. (2016) and in McQuillan et al. (2013), where the slope of the upper envelope of the period-mass relation changes sign around $0.55 M_{\odot}$, below which period rises with decreasing mass, an uncertainty (or a systematic shift) of $\sim 20\%$ on mass could match these disagreement.

In Fig. 13, we draw the signal amplitudes distributions from *Kepler* and APACHE rotators. Looking at the APACHE distribution, we note how we do not observe semi-amplitudes below 2.5 mmag. This is probably due to the survey sensitivity limit over an observation season. Based on a new K-S test, we obtain $p_{K-S} = 0.815$, showing that

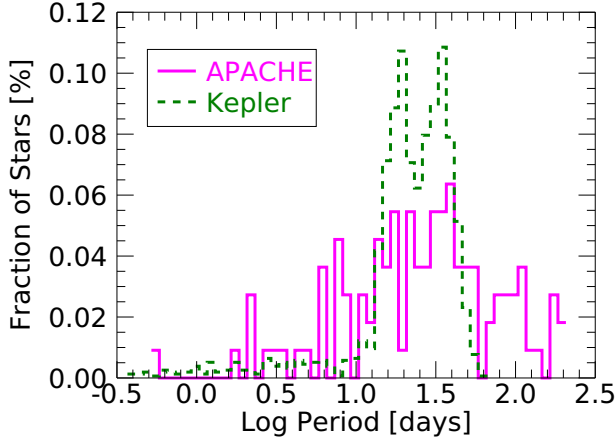


Figure 12. Fraction of stars as a function of the logarithm of the rotation period (expressed in days). The red solid line draw the APACHE period distribution while the green dashed line draw the Kepler period distribution.

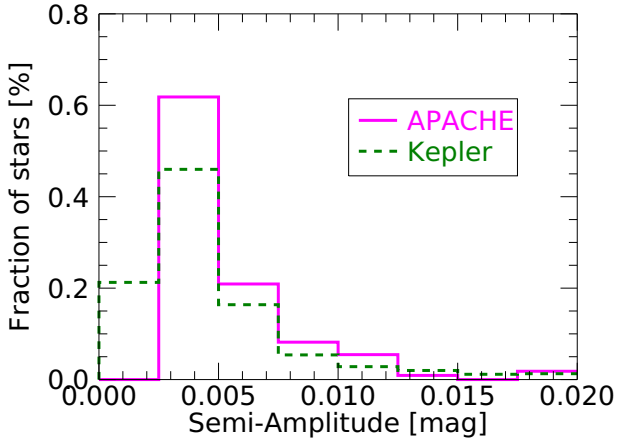


Figure 13. Fraction of stars as a function of signal semi-amplitude in magnitude. The red solid line drawn the APACHE distribution while the green dashed line drawn the Kepler distribution.

Kepler and APACHE semi-amplitude distributions are consistent with the samples being drawn from the same cumulative distribution function. It is important to note that the photometric band-pass of the *Kepler* survey is different from that of the APACHE survey. The direct consequence of observing at different wavelengths is to obtain different contrast between spotted and unspotted photosphere and, consequently, a different amplitude of the modulation.

5.3 Comparison with rotation periods from MEarth North & South

Since in Sec. 4.3, we used the MEarth Irwin et al. (2011) sample to show how the properties in terms of kinematic of the two samples are substantially equivalent, here we use the

complete sample of late type M dwarfs from Newton et al. (2016) and Newton et al. (2018) to compare the late M dwarfs mass-period relation from MEarth to the early M dwarfs mass period relation from APACHE and Kepler surveys. Since APACHE and Kepler surveys both have a star mass distribution that peaks at $0.5 M_{\odot}$, while MEarth has a mass distribution that peaks at $0.2 M_{\odot}$, this is a good opportunity to bridge the two samples over the full range of M dwarf masses. As highlighted in Sec. 3.3, the masses for MEarth and Kepler are determined using different methods with respect to this work and do not benefit of the *Gaia* DR2 data, so there may be an offset between the two mass scales and the APACHE one. In any case, an exact review of the masses is beyond the scope of this work and these uncertainties do not heavily affect the statistical considerations presented here.

In Tab. 3 we summarize the property of APACHE, *Kepler* and MEarth samples.

In Fig. 14 we show the rotation period distribution for the APACHE, *Kepler* and MEarth surveys. While the APACHE sample, supported by *Kepler* data, shows a single peak around ~ 30 days, the MEarth period distribution appears to be in two clumps, a population of rapidly rotating objects with periods of ≈ 0.2 -10 days, and a population of slowly rotating objects with periods of ≈ 30 -160 days. The APACHE period distribution has a bigger variance with respect to the *Kepler* or MEarth slow rotation period distributions, due to the bigger variance of the APACHE mass distribution. It is interesting to note in Fig. 14 that while for the early M dwarfs samples from APACHE and *Kepler* the shorter periods look like a tail in the period distributions, we see a gap between “slow” and “fast” rotators in the period distributions for the late M dwarf stars from MEarth.

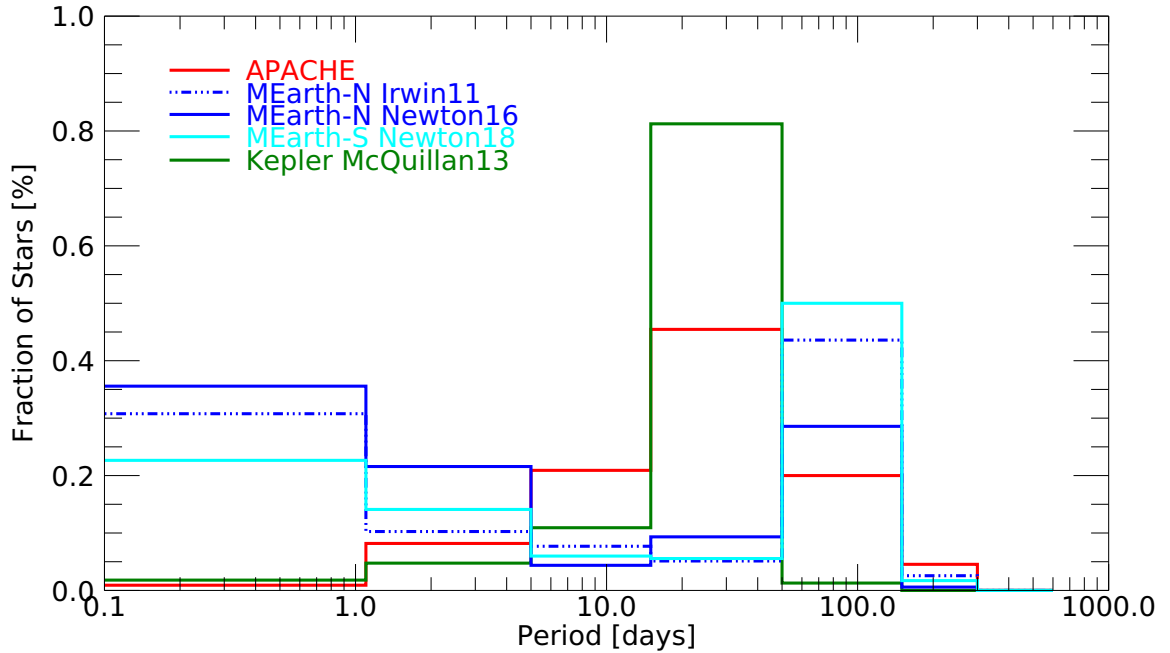
In Fig. 15 we show the rotation period as a function of the stellar masses for the APACHE, *Kepler* and MEarth surveys. First of all, there is a clear dependence on the stellar mass for slow rotators over the full mass range, with the lowest-mass stars reaching the longest rotation periods. Furthermore, the two clumps in the MEarth periods distribution described above are here well visible in the mass range 0.1 - $0.3 M_{\odot}$ where $\sim 50\%$ of the lowest-mass stars show the fastest rotation rates. Moreover, the gap between “slow” and “fast” rotators increases with decreasing mass.

The rotation periods we find for the APACHE M dwarfs are consistent with the MEarth results for the older/slow rotators stars and in the overlapping mass range between APACHE and MEarth. The lack of fast rotators between APACHE/*Kepler* and MEarth could be principally due to the fact that APACHE and *Kepler* do not observe M dwarf stars below the full convection limit around $\sim 0.3 M_{\odot}$.

As described in Sec. 3.1, during the initial target selection we cross-correlated our sample with many catalogs, searching for additional information such as measurements of projected rotational velocity $V \sin i$ and level of chromospheric activity and X-ray emission, to flag active targets. We suggest that the impact of this initial selection on the observational strategy was very limited for two reasons: 1) the number of fast rotator/active stars excluded based on the cross match was only on the order of 1% of the full APACHE sample; 2) the final ranking was dominated by parameters such as observability, the number of *Gaia* observations and the ongoing HADES spectroscopic monitor-

Table 3. Summary of rotation sample properties from APACHE, *Kepler* and MEarth surveys

Survey	Reference paper	Stars with measured rotation #	Stars sample #	Period Range (days)	Mass Range (M_{\odot})
APACHE	this work	107	247	0.1-135	0.18-0.79
<i>Kepler</i>	McQuillan et al. (2013)	1570	2483	0.37-67	0.3-0.55
MEarth-N	Irwin et al. (2011)	41	273	0.28-154	0.025-0.35
MEarth-N	Newton et al. (2016)	387	1883	0.1-140	0.06-0.78
MEarth-S	Newton et al. (2018)	234	574	0.1-149	0.08-0.38

**Figure 14.** Fraction of stars as a function of rotation period. The red solid line draws the APACHE distribution, the blue dash-dotted line indicates the Irwin et al. (2011) period distribution, the blue solid line draws the MEarth-North period distribution from Newton et al. (2016), the light blue solid line indicates the MEarth-South period distribution from Newton et al. (2018) while the green solid line draws the *Kepler* period distribution from McQuillan et al. (2013).

ing. Therefore, although there may be a slight bias against fast rotators, we think the impact on the final distribution is very low. This is confirmed by the excellent agreement with the *Kepler* survey period distribution, where a possible pre-selection against active stars/fast rotators is even more limited.

6 SUMMARY AND DISCUSSION

We searched for photometric rotation periods of 247 M dwarfs in the mass range $0.15 - 0.70M_{\odot}$ observed by the APACHE transit survey during five years of operations. When searching for sinusoidal signals in the data, we used GLS to calculate the frequency periodogram sampled on a uniform grid in frequency from 0.1 to 500 days. We estimated the significance of the highest GLS peaks with a bootstrap analysis and we selected as candidate rotators all the objects with FAP $\leq 1\%$, a semi-amplitude of the signal ≥ 2.5

mmag, and after a visual inspection. The final sample consists of 107 M dwarfs with rotation periods in the range $0.52 - 191.82$ days, with a peak in distribution at ~ 30 days. We performed a simulation to test our survey sensitivity, and we quantified the loss of detection efficiency at long periods. This is an expected result due to the limited duration of the time series, the instrumental instability over five years and the intrinsic variation of stellar spots which we do not take into account in the period search. In spite of this, we found that our period distribution is substantially unbiased in the period range $0.5 - 200$ days. Looking at the rotation period-mass relation and excluding the fast rotators with $P < 10$ days, the period appears mass dependent, increasing with decreasing mass. Moreover, for our sample of early M dwarfs, we found that the amplitude of variability is not correlated with the rotation period.

This catalogue of 107 M dwarfs with a measured rotation period bears potential for important contributions to the analysis of space-based photometric data from tran-

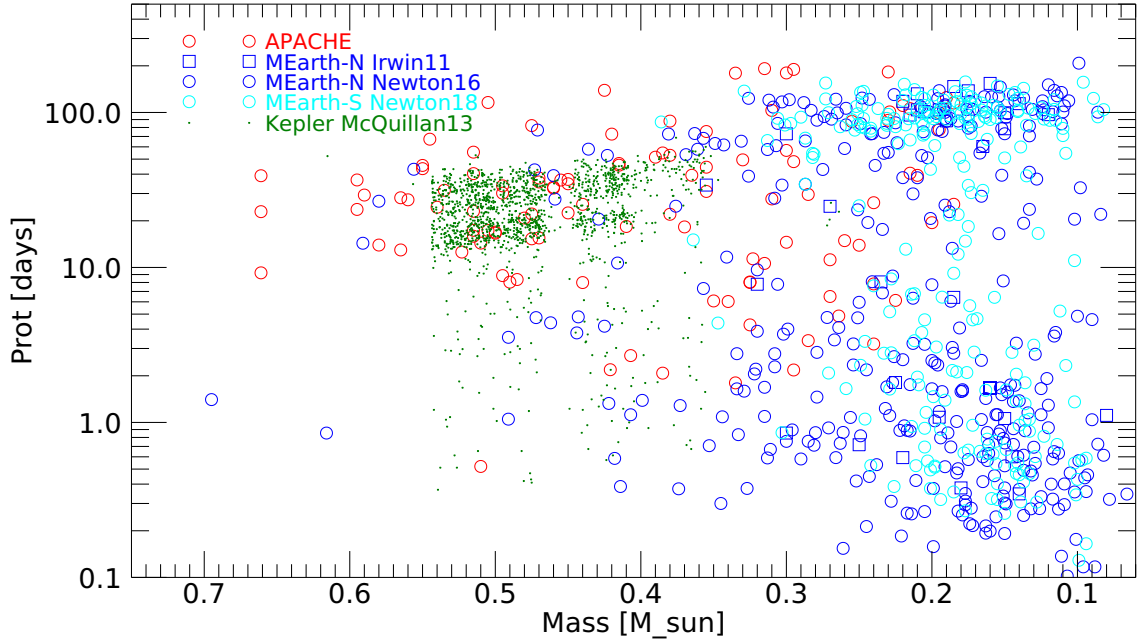


Figure 15. Rotation period as a function of stellar mass. The red circles represent the APACHE data, the blue squares represent the Irwin et al. (2011) data, the blue circles the MEarth-North data from Newton et al. (2016), the light blue circles represent the MEarth-South period distribution from Newton et al. (2018) while the green dots represent the *Kepler* data from McQuillan et al. (2013).

sit detection and characterization missions such as TESS, PLATO, CHEOPS, and ARIEL. In particular, in the presence of small-size transit candidates (of potential interest for atmospheric characterization too) our results might be useful in disentangling planetary signals (be they dynamical or atmospheric) from those related to stellar magnetic activity.

While the primary focus of this work is on the measurement of robust rotation periods of the APACHE sample of M dwarfs, it is nevertheless possible to comment on the statistics of the results obtained in the context of relevant aspects of the astrophysics of cool stars.

We compared the rotation period of 23 APACHE targets with the rotation period derived spectroscopically by the HADES program. We see that for most stars there is a good correspondence between either the two rotation periods or one rotation period and the first harmonic of the other. Moreover, we compared our rotation period distribution with the distribution from 1570 rotating M dwarfs in the mass range $0.3 - 0.55 M_{\odot}$ observed by the *Kepler* survey. The two distributions are in good agreement with the peak that lies around ~ 30 days and a tail of fast rotators with $P < 10$ days. The comparison of our rotation periods to the spectroscopic periods from the literature and the comparison between our period distribution with the one from the *Kepler* survey give support to the periods we detected, although we refer the reader to Sec. 5.1 and Sec. 5.2 for the details.

We used the *Gaia* DR2 to characterize the Galactic kinematics for our M dwarfs with measured rotation. We

found that our sample has kinematics consistent with the stellar number density distribution of the Milky Way in the Solar neighborhood. Furthermore, we tested our kinematic characterization on the sub-sample of the late M dwarfs presented in Irwin et al. (2011). We can broadly group our rotating sample by their kinematics into the thin and thick disk galaxy population. This classification was used as a proxy for stellar age. While the thin disk sample spans the full range of periods and includes entirely the rapidly rotating objects, the thick disk sample is constituted only by slowly rotating stars. Similarly to the thin disk sample, the stars with an intermediate kinematics classification span the full range of periods, but with no objects in the ultra fast ($P < 5$ days) rotating clump. Given the mean old age of the thick disk (~ 10 Gyr), this suggests that the older objects in the sample are rotating more slowly. Based on a Spearman rank correlation test, that returned a value of the correlation coefficient of 0.22 ± 0.03 , we confirmed a (weak) correlation between the space velocity dispersion and the rotation period.

Assuming that the velocity dispersion increases with age, as expected for older stellar population, the star's ages are increasing with rotation period. We investigated this aspect considering the velocity dispersion-age relation in the V_Z velocity component, which is the most sensitive to age. For our most populated bin with period $10 < P < 70$ days, we found a mean age of 3.3 ± 0.6 Gyr. We are not able to really constrain the ages of the other bins, due to the small size of our sample. Comparing this result with the one published

by Newton et al. (2016), in which a mean age of $4.5_{-2.3}^{+3.9}$ Gyr was found for the period bin $P > 70$ days, we confirm that late M dwarfs spin down to longer periods than early M dwarfs.

Despite the good agreement between the two works, there is a question still unresolved: the lack of fast rotators ($P < 10$ days) in the APACHE/Kepler sample. This could be explained with an observational bias in the target selection with no “young” stars (age < 1 Gyr). In any case, we prioritized our targets mostly on observational constraints and taking into account the number of *Gaia* transits, therefore our sample should not be astrophysically biased. Over an initial sample of ~ 3000 M dwarfs only a handful of stars have been excluded as suspect young and over-active. This is more true for the *Kepler* sample where it is difficult to imagine an observational bias based on the age/activity because of the lack of archive information for this type of stars due to their lower intrinsic luminosity. On the other hand, we could assume an incorrect estimate of the mean age of late type M dwarf fast rotators or, symmetrically, a very different time scale in the rotation period evolution between early and late type stars. In this case, we assume that the late M dwarfs are maintaining rapid rotation for longer than their early counterparts or, symmetrically, the early M dwarfs spin down faster than their late counterparts. Indeed, the increase in the fraction of rapid rotators with decreasing stellar mass, with a particularly sharp increase in fast rotators at around $\sim 0.3 M_{\odot}$ (which corresponds to the transition to fully convective stellar interiors) has recently been noticed by others (e.g., Gilhool et al. 2018, and references therein). The more natural explanation for this bimodality calls into question the effectiveness with which fully convective stars, late-type stars are capable of releasing angular momentum in comparison with earlier-type stars with radiative cores.

ACKNOWLEDGEMENTS

P.G. acknowledges financial support from the Italian Space Agency (ASI) under contract 2014-025-R.1.2015 to INAF; M.D. acknowledges financial support from Progetto Premiale 2015 FRONTIERA funding scheme of the Italian Ministry of Education, University, and Research; M.Pi. gratefully acknowledges the support from the European Union Seventh Framework Programme (FP7/2007-2013) under Grant Agreement No. 313014 (ETA-EARTH); D.B. acknowledges financial support from INAF and Agenzia Spaziale Italiana (ASI grant no. 2014-025-R.1.2015) for the 2016 Ph.D. fellowship programme of INAF; EP acknowledges the financial support of the 2014 PhD fellowship programme of the INAF; The Astronomical Observatory of the Autonomous Region of the Aosta Valley (OAVdA) is managed by the Fondazione Clément Fillietroz-ONLUS, which is supported by the Regional Government of the Aosta Valley, the Town Municipality of Nus and the “Unité des Communes valdôtaines Mont-Émilium”. The authors thank ASI (through contracts I/037/08/0 and I/058/10/0) and Fondazione CRT for their support to the APACHE Project; We acknowledge R. Smart, B. Bucciarelli and A. Spagna for interesting and useful discussions on various aspects of this work; P.G. acknowledges Ilaria Carleo for unique conversations and contributions during the manuscript draft.

REFERENCES

- Affer L., et al., 2016, *A&A*, **593**, A117
 Affer L., et al., 2019, *A&A*, **622**, A193
 Anglada-Escudé G., Tuomi M., 2015, *Science*, **347**, 1080
 Anglada-Escudé G., et al., 2016a, *Nature*, **536**, 437
 Anglada-Escudé G., et al., 2016b, *ApJ*, **830**, 74
 Astudillo-Defru N., Delfosse X., Bonfils X., Forveille T., Lovis C., Rameau J., 2017a, *A&A*, **600**, A13
 Astudillo-Defru N., et al., 2017b, *A&A*, **602**, A88
 Astudillo-Defru N., et al., 2017c, *A&A*, **605**, L11
 Aumer M., Binney J. J., 2009, *MNRAS*, **397**, 1286
 Bailer-Jones C. A. L., 2015, *PASP*, **127**, 994
 Bakos G. Á., 2018, The HATNet and HATSouth Exoplanet Surveys. p. 111, doi:10.1007/978-3-319-55333-7-111
 Ballard S., 2019, *AJ*, **157**, 113
 Barclay T., Pepper J., Quintana E. V., 2018, *ApJS*, **239**, 2
 Barnes S. A., 2007, *ApJ*, **669**, 1167
 Benatti S., et al., 2016, in *Frontier Research in Astrophysics II*. p. 69 (arXiv:1708.04166)
 Berger T. A., Huber D., Gaidos E., van Saders J. L., 2018, *The Astrophysical Journal*, **866**, 99
 Berta Z. K., Irwin J., Charbonneau D., Burke C. J., Falco E. E., 2012, *The Astronomical Journal*, **144**, 145
 Bonfils X., et al., 2013, *A&A*, **549**, A109
 Bonfils X., et al., 2018, *A&A*, **613**, A25
 Burke C. J., Gaudi B. S., DePoy D., Pogge R. W., 2006, *The Astronomical Journal*, **132**, 210
 Carolo E., et al., 2014, *A&A*, **567**, A48
 Chen B., et al., 2001, *ApJ*, **553**, 184
 Christille J.-M., et al., 2013, in *EPJ Web of Conferences*. p. 17001
 Cloutier R., Doyon R., Menou K., Delfosse X., Dumusque X., Artigau É., 2017, *AJ*, **153**, 9
 Collier Cameron A., et al., 2009, *MNRAS*, **400**, 451
 Damasso M., Giacobbe P., Calciolone P., Sozzetti A., Lattanzi M. G., Bernagozzi A., Bertolini E., Smart R. L., 2010, *PASP*, **122**, 1077
 Damasso M., et al., 2018, *A&A*, **615**, A69
 Damasso M., Pinamonti M., Scandariato G., Sozzetti A., 2019, *MNRAS*, **489**, 2555
 Desidera S., et al., 2014, *A&A*, **567**, L6
 Dittmann J. A., et al., 2017, *Nature*, **544**, 333
 Dressing C. D., Charbonneau D., 2015, *ApJ*, **807**, 45
 Drimmel R., Poggio E., 2018, *Research Notes of the American Astronomical Society*, **2**, 210
 Endl M., et al., 2016, *ApJ*, **818**, 34
 Feltzing S., Bensby T., 2008, *Physica Scripta Volume T*, **133**, 014031
 Foreman-Mackey D., Montet B. T., Hogg D. W., Morton T. D., Wang D., Schölkopf B., 2015, *The Astrophysical Journal*, **806**, 215
 Gaia Collaboration et al., 2018, *A&A*, **616**, A11
 Giacobbe P., et al., 2012, *Monthly Notices of the Royal Astronomical Society*, **424**, 3101
 Gilhool S. H., Blake C. H., Terrien R. C., Bender C., Mahadevan S., Deshpande R., 2018, *AJ*, **155**, 38
 Gilliland R. L., Chaplin W. J., Jenkins J. M., Ramsey L. W., Smith J. C., 2015, *AJ*, **150**, 133
 González-Álvarez E., et al., 2019, *A&A*, **624**, A27
 Gravity Collaboration et al., 2018, *A&A*, **615**, L15
 Hardegree-Ullman K. K., Cushing M. C., Muirhead P. S., Christiansen J. L., 2019, arXiv e-prints, p. arXiv:1905.05900
 Hartman J. D., et al., 2009, *ApJ*, **691**, 342
 Haywood R. D., et al., 2014, *MNRAS*, **443**, 2517
 Herbst W., Bailer-Jones C. A. L., Mundt R., Meisenheimer K., Wackermann R., 2002, *A&A*, **396**, 513
 Hobson M. J., et al., 2019, *A&A*, **625**, A18

- Irwin J., Berta Z. K., Burke C. J., Charbonneau D., Nutzman P., West A. A., Falco E. E., 2011, *ApJ*, **727**, 56
- Jurić M., et al., 2008, *ApJ*, **673**, 864
- Kaltenegger L., Pepper J., Stassun K., Oelkers R., 2019, *ApJ*, **874**, L8
- Kopparapu R. K., 2018, The Habitable Zone: The Climatic Limits of Habitability. p. 58, doi:10.1007/978-3-319-55333-7_58
- Kopparapu R. K., et al., 2013, *ApJ*, **765**, 131
- Kopparapu R. K., Ramirez R. M., SchottelKotte J., Kasting J. F., Domagal-Goldman S., Eymet V., 2014, *ApJ*, **787**, L29
- Kovács G., Bakos G., Noyes R. W., 2005, Monthly Notices of the Royal Astronomical Society, 356, 557
- Kubánek P., 2010, Advances in Astronomy, 2010
- Lépine S., Gaidos E., 2011, *AJ*, **142**, 138
- Luque R., et al., 2018, *A&A*, **620**, A171
- McQuillan A., Aigrain S., Mazeh T., 2013, *MNRAS*, **432**, 1203
- Mortier A., Collier Cameron A., 2017, *A&A*, **601**, A110
- Newton E. R., Irwin J., Charbonneau D., Berta-Thompson Z. K., Dittmann J. A., West A. A., 2016, *ApJ*, **821**, 93
- Newton E. R., Mondrik N., Irwin J., Winters J. G., Charbonneau D., 2018, *AJ*, **156**, 217
- Nissen P. E., 2004, Origin and Evolution of the Elements, p. 154
- Nutzman P., Charbonneau D., 2008, *PASP*, **120**, 317
- Perger M., et al., 2017, *A&A*, **598**, A26
- Pinamonti M., et al., 2019, *A&A*, **625**, A126
- Pollacco D. L., et al., 2006, *PASP*, **118**, 1407
- Prosser C. F., et al., 1995, *PASP*, **107**, 211
- Ricker G. R., et al., 2014, in Proc. SPIE. p. 914320 (arXiv:1406.0151), doi:10.1117/12.2063489
- Robertson P., Mahadevan S., Endl M., Roy A., 2014, *Science*, **345**, 440
- Robertson P., Roy A., Mahadevan S., 2015, *ApJ*, **805**, L22
- Schönrich R., Binney J., Dehnen W., 2010, *MNRAS*, **403**, 1829
- Sozzetti A., et al., 2013, in EPJ Web of Conferences. p. 03006
- Spada F., Demarque P., Kim Y. C., Sills A., 2013, *ApJ*, **776**, 87
- Spada F., Demarque P., Kim Y. C., Boyajian T. S., Brewer J. M., 2017, *ApJ*, **838**, 161
- Suárez Mascareño A., Rebolo R., González Hernández J. I., Esposito M., 2015, *MNRAS*, **452**, 2745
- Suárez Mascareño A., Rebolo R., González Hernández J. I., 2016, *A&A*, **595**, A12
- Suárez Mascareño A., et al., 2017a, *A&A*, **605**, A92
- Suárez Mascareño A., et al., 2017b, *A&A*, **605**, A92
- Suárez Mascareño A., et al., 2018, *A&A*, **612**, A89
- Sullivan P. W., et al., 2015, *ApJ*, **809**, 77
- Vanderburg A., Plavchan P., Johnson J. A., Ciardi D. R., Swift J., Kane S. R., 2016, *MNRAS*, **459**, 3565
- Wright N. J., Newton E. R., Williams P. K. G., Drake J. J., Yadav R. K., 2018, *MNRAS*, **479**, 2351
- Young A. T., 1967, *AJ*, **72**, 747
- Yu J., Liu C., 2018, *MNRAS*, **475**, 1093
- Zechmeister M., Kürster M., 2009, *A&A*, **496**, 577
- Zechmeister M., et al., 2019, arXiv e-prints, p. arXiv:1906.07196

APPENDIX A: TABLES

Table A1: Observational Properties for the APACHE stars.

Name	RA (deg)	Dec (deg)	V (mag)	N points	N nights	ΔHJD (days)	σ_r (mag)	Φ_{det} (%)	$\Phi_{det,h}$ (%)	Rotator Yes/No
J00156+7217	3.902023	72.283562	12.70	4798	108	814.	0.0045	82	0	Y
J00166+3000	4.168521	30.016624	12.79	1772	39	481.	0.0046	50	7	Y
J00207+5936	5.198862	59.604836	12.80	4935	138	798.	0.0036	99	0	Y
J00234+7711	5.870607	77.189285	11.31	3718	99	618.	0.0052	86	0	Y
J00374+5133	9.358173	51.552032	11.54	3168	103	1148.	0.0043	94	0	Y
J01013+6121	15.333420	61.365776	10.92	4737	69	197.	0.0083	61	0	Y
J01025+7140	15.633533	71.679871	9.98	4310	96	1538.	0.0039	100	0	Y
J01056+2829	16.406815	28.492657	15.64	3159	82	800.	0.0040	99	0	Y
J02155+3357	33.893379	33.961407	14.07	3935	94	1634.	0.0040	99	0	Y
J02207+3044	35.179794	30.745981	12.37	1633	34	1603.	0.0055	48	10	Y
J02565+5526S	44.143288	55.437317	10.73	5940	125	1600.	0.0055	99	0	Y
J02592+3146	44.819622	31.773594	13.89	683	19	1593.	0.0045	43	19	Y
J03122+2951	48.052689	29.859001	11.28	6626	137	1538.	0.0055	98	0	Y
J03437+1640	55.938515	16.667305	10.83	176	11	472.	0.0050	12	40	Y
J04086+3338	62.155735	33.637020	10.18	2558	42	524.	0.0101	21	17	Y
J04129+5236	63.244991	52.611649	13.80	1923	53	426.	0.0109	38	14	Y
J04199+3629	64.998680	36.486546	11.46	2190	63	877.	0.0060	80	0	Y
J04248+3226	66.204872	32.449459	11.98	1808	56	1636.	0.0054	83	5	Y
J04414+1313	70.373688	13.221195	11.26	1080	23	68.	0.0042	56	25	Y
J04525+4042	73.144196	40.706730	13.56	3359	80	560.	0.0048	95	0	Y
J05198+3159	79.971581	31.992743	13.39	3678	97	1266.	0.0061	93	0	Y
J05298+3204	82.469398	32.080883	12.77	2418	55	526.	0.0050	99	0	Y
J05334+4809	83.371078	48.157131	11.68	1905	60	787.	0.0050	78	2	Y
J06140+5140	93.509834	51.668896	13.40	4803	118	1487.	0.0053	99	0	Y
J06147+4727	93.676758	47.459602	11.56	7988	171	1431.	0.0045	99	0	Y
J06162+7722	94.059441	77.382080	13.82	2843	70	423.	0.0050	87	0	Y
J06170+8353	94.272034	83.893135	13.57	2976	64	830.	0.0188	57	18	Y
J06194+1357	94.872879	13.950819	10.93	1566	30	462.	0.0048	53	4	Y
J07044+6817	106.107964	68.288795	11.95	5084	115	1649.	0.0065	100	0	Y
J07086+3042	107.164711	30.713886	11.54	1719	32	420.	0.0063	50	7	Y
J07316+6201W	112.900566	62.019855	11.96	6405	140	1331.	0.0040	100	0	Y
J08315+7303	127.875351	73.062737	13.42	3756	80	1209.	0.0047	87	0	Y
J08321+8424	128.041870	84.408592	13.79	6011	126	1599.	0.0054	99	0	Y
J08376+3156	129.413803	31.948244	12.88	955	23	99.	0.0043	66	19	Y
J08507+3505	132.687225	35.084469	12.68	4874	125	1243.	0.0041	100	0	Y
J09014+2957	135.371277	29.952942	13.74	735	21	384.	0.0048	23	27	Y
J09108+3127	137.701248	31.457430	13.95	1304	35	426.	0.0039	57	13	Y
J09133+6852	138.349335	68.875160	11.23	4649	99	1328.	0.0045	100	0	Y
J09327+8208	143.185806	82.139236	12.75	4639	92	497.	0.0045	80	0	Y
J10312+8139	157.808640	81.663597	13.00	2576	78	363.	0.0044	79	0	Y
J10506+5145	162.659332	51.750435	14.72	3076	85	829.	0.0036	91	0	Y
J10558+5602	163.959259	56.037186	12.95	2749	102	1639.	0.0042	100	0	Y
J10567+4313	164.190811	43.233173	12.93	1242	34	857.	0.0046	91	2	Y
J11000+2249	165.018017	22.833138	0.00	4204	96	1127.	0.0037	98	0	Y
J11009+2800	165.233536	28.011812	12.84	2026	70	1520.	0.0057	94	0	Y
J11026+2158	165.659757	21.967139	0.00	2672	59	477.	0.0036	86	0	Y
GJ3649	168.162452	18.934843	0.00	3839	82	1127.	0.0043	97	0	Y
J11254+7815	171.372787	78.265739	12.19	3183	123	561.	0.0047	89	0	Y
J11298+3606	172.468048	36.111515	13.69	707	22	857.	0.0058	22	16	Y
J11318+2725	172.974854	27.426025	14.22	793	24	1476.	0.0060	16	17	Y
J11379+2951	174.494247	29.855530	13.73	2852	79	864.	0.0053	86	0	Y
J11511+3516	177.780572	35.272015	0.00	774	33	743.	0.0052	50	13	Y
J11529+2428	178.241241	24.479298	14.73	2269	86	1496.	0.0052	98	0	Y
J11582+4234	179.573395	42.574711	14.43	2728	89	1519.	0.0038	100	0	Y
J12194+2822	184.850370	28.382366	0.00	2865	19	66.	0.0041	59	22	Y
J12194+2822	184.850370	28.382366	0.00	750	22	152.	0.0040	51	7	Y
J12253+3743	186.346085	37.724266	11.90	2899	74	816.	0.0043	92	0	Y
J12274+3726	186.872620	37.442604	12.08	2960	80	1536.	0.0048	98	0	Y
J12350+0949	188.753006	9.828533	11.40	1259	35	512.	0.0048	67	2	Y
J12505+2655	192.644043	26.923075	14.17	1022	25	440.	0.0055	33	13	Y
J13436+3321	205.924271	33.355385	12.75	901	35	482.	0.0049	50	8	Y
J13517+3142	207.938049	31.716021	13.40	2743	92	890.	0.0050	98	1	Y
J13580+3141	209.506790	31.695421	12.68	1076	28	115.	0.0036	52	18	Y
J14257+2337W	216.431030	23.617239	0.00	471	46	1147.	0.0036	86	6	Y

Table A1: Continued.

Name	RA (deg)	Dec (deg)	V (mag)	N points	N nights	ΔHJD (days)	σ_r (mag)	Φ_{det} (%)	$\Phi_{det,h}$ (%)	Rotator Yes/No
J14294+1531	217.373744	15.532639	0.00	2669	76	1124.	0.0034	99	0	Y
J15297+4252	232.433258	42.880249	14.64	3395	116	768.	0.0037	98	0	Y
J15336+4615	233.413879	46.250866	14.03	1687	86	1533.	0.0049	90	5	Y
J16008+4019	240.211655	40.328773	13.59	4152	148	901.	0.0052	100	0	Y
J16072+2650	241.806839	26.838085	13.50	4134	110	1511.	0.0056	97	1	Y
J16254+5418	246.352597	54.304104	0.00	2450	96	1064.	0.0039	94	0	Y
J16259+8324	246.493179	83.406700	12.22	6627	224	1330.	0.0041	100	0	Y
J16408+3619	250.203705	36.316692	11.48	3979	128	908.	0.0050	99	0	Y
J16420+1916	250.503113	19.269569	12.70	1244	50	1117.	0.0047	79	4	Y
J17104+2758W	257.606079	27.977779	13.13	1048	48	339.	0.0039	66	2	Y
J17158+1900	258.958801	19.000015	10.73	1458	52	636.	0.0058	50	7	Y
J17160+1103	259.002645	11.057621	0.00	3973	93	1087.	0.0099	50	15	Y
J17166+0803	259.170807	8.058401	11.49	3034	92	1526.	0.0053	90	2	Y
J17312+8205	262.821533	82.088921	14.09	5508	114	620.	0.0053	85	0	Y
J17378+1835	264.472279	18.591711	0.00	1457	50	461.	0.0053	38	8	Y
J17395+2745	264.877991	27.762253	11.07	1176	31	40.	0.0074	10	19	Y
J17589+8042	269.736176	80.712204	13.20	2835	110	516.	0.0055	81	0	Y
J18234+2810	275.868103	28.167734	12.32	2452	74	1152.	0.0068	72	9	Y
J18353+4544	278.826627	45.744042	0.00	5903	163	1252.	0.0032	100	0	Y
J18563+5429W	284.075897	54.497581	11.74	1836	55	851.	0.0048	85	1	Y
J18580+0554	284.500569	5.908118	0.00	3449	81	765.	0.0048	76	11	Y
J18596+0759	284.910828	7.987281	10.86	1701	63	367.	0.0050	49	5	Y
J19242+7943	291.063263	79.726883	11.45	5793	172	1449.	0.0047	99	0	Y
J19540+3233	298.511108	32.564766	12.26	701	31	1776.	0.0050	33	13	Y
J20586+3416	314.674683	34.274200	11.21	1322	39	467.	0.0047	64	7	Y
J21012+3314	315.317108	33.242439	12.25	2184	59	518.	0.0073	58	5	Y
J21109+2925	317.728241	29.423113	11.06	4184	127	814.	0.0050	86	0	Y
J21129+3107E	318.231049	31.131737	11.84	4652	159	1363.	0.0053	97	0	Y
J21152+2547	318.802429	25.795969	11.92	3572	91	1554.	0.0060	89	0	Y
J21179+3404	319.496124	34.075050	11.91	4411	145	911.	0.0045	100	0	Y
J21185+3014	319.640625	30.242956	0.00	496	38	419.	0.0046	51	11	Y
J21185+3014	319.640625	30.242956	11.87	3148	112	1350.	0.0034	92	0	Y
J21366+3927E	324.160767	39.455730	10.17	5891	160	1146.	0.0058	98	0	Y
J21487+4019	327.193573	40.328461	11.27	1768	47	96.	0.0049	56	22	Y
J22006+2715	330.173309	27.253777	11.53	1070	36	880.	0.0044	60	3	Y
J22107+0754	332.686218	7.909122	10.92	4543	145	1576.	0.0053	94	1	Y
J22129+5504N	333.236664	55.080524	11.02	953	30	60.	0.0055	34	25	Y
J22154+6613	333.859009	66.224350	13.91	384	21	452.	0.0093	7	38	Y
J22385+8309	339.636505	83.166664	12.70	2890	93	1152.	0.0044	91	0	Y
J22562+5919	344.056244	59.319046	11.60	283	11	62.	0.0037	9	25	Y
J23182+7934	349.570465	79.579865	14.40	4656	110	908.	0.0028	95	0	Y
J23313+5944	352.832245	59.747662	9.90	3371	60	159.	0.0101	24	27	Y
J23428+3049	355.719727	30.822731	14.66	1134	36	489.	0.0035	72	4	Y
J23513+2344	357.842926	23.739084	14.16	1749	33	59.	0.0052	42	25	Y
J23515+3127	357.890320	31.456356	13.65	638	15	45.	0.0043	35	27	Y
J00051+4547	1.295195	45.786587	9.95	4647	79	540.	0.0113	75	2	N
J00113+5837	2.841032	58.617561	11.21	4418	67	163.	0.0078	57	0	N
J00119+3303	2.985193	33.054703	13.40	3373	92	1422.	0.0038	95	0	N
J00232+5445	5.812493	54.752010	11.75	1673	59	763.	0.0036	82	0	N
J00409+3122	10.234305	31.382376	13.88	2958	93	1595.	0.0057	96	0	N
J00508+3308	12.708258	33.143459	12.87	4330	111	1008.	0.0039	96	0	N
J00558+3100	13.962433	31.007284	12.22	962	23	449.	0.0042	54	6	N
J01012+2901N	15.323452	29.033249	14.00	294	8	410.	0.0055	0	24	N
J01161+6009	19.042156	60.153561	11.42	2773	59	159.	0.0070	64	0	N
J01198+8409	19.967289	84.159134	14.85	2865	85	999.	0.0039	88	0	N
J01514+2123	27.850719	21.394299	14.41	454	15	385.	0.0038	30	32	N
J01518+6426	27.963015	64.434998	11.65	4799	131	1677.	0.0053	98	0	N
J02015+6346	30.397266	63.770027	11.13	5884	95	421.	0.0056	69	0	N
J02115+2046	32.899788	20.778610	11.99	461	17	1545.	0.0059	6	30	N
J02207+3044	35.179794	30.745981	0.00	5992	19	59.	0.0043	56	20	N
J02358+2013	38.972080	20.219902	10.68	1194	24	407.	0.0097	6	28	N
J02565+5526N	44.146698	55.441643	10.99	4040	81	421.	0.0052	87	0	N
J03147+4831	48.687126	48.519733	11.50	804	21	1585.	0.0054	29	25	N
J03207+3943	50.188370	39.717091	11.22	6254	117	1205.	0.0050	100	0	N

Table A1: Continued.

Name	RA (deg)	Dec (deg)	V (mag)	N points	N nights	ΔHJD (days)	σ_r (mag)	Φ_{det} (%)	$\Phi_{det,h}$ (%)	Rotator Yes/No
J03280+2201	52.009628	22.023123	11.41	195	10	145.	0.0039	4	42	N
J03416+5513	55.405293	55.218575	11.34	6751	172	1184.	0.0053	100	0	N
J03454+7259N	56.366440	72.992310	11.86	4183	86	789.	0.0091	71	8	N
J03466+8207	56.674992	82.130890	11.99	2895	64	893.	0.0115	36	26	N
J03567+5333	59.197422	53.560253	10.86	4007	102	1478.	0.0065	97	0	N
J04129+5236	63.244991	52.611649	0.00	1278	21	43.	0.0047	44	22	N
J04545+3729	73.633278	37.497746	10.25	5463	123	1478.	0.0042	97	0	N
J04587+5056	74.691521	50.943871	10.97	1781	48	687.	0.0072	67	4	N
J05033+5307	75.849289	53.128681	9.96	1793	48	1260.	0.0052	61	2	N
J05076+2730	76.902779	27.501524	11.56	933	22	124.	0.0040	57	24	N
J05173+3207	79.333221	32.126240	13.48	4887	127	1488.	0.0057	99	0	N
J05173+7210	79.338623	72.180962	12.19	6455	100	798.	0.0038	96	0	N
J05181+3224	79.527832	32.411381	11.77	558	22	1624.	0.0051	18	15	N
J05341+5112	83.536110	51.215683	11.07	7423	180	1502.	0.0056	99	0	N
J05466+4407	86.660149	44.122147	13.03	578	14	1581.	0.0059	1	35	N
J05468+6630	86.703011	66.503220	11.77	848	24	127.	0.0057	20	43	N
J05532+2415	88.308601	24.258806	10.98	1523	36	354.	0.0079	38	2	N
J05558+4036	88.951698	40.613838	12.06	3428	71	755.	0.0090	56	6	N
J05558+6625	88.953987	66.427010	12.36	6880	148	1375.	0.0034	99	0	N
J06007+6808	90.194061	68.141396	13.36	270	22	1586.	0.0059	6	34	N
J06011+7557	90.275070	75.951942	12.75	4661	89	837.	0.0047	89	0	N
J06071+3332	91.799133	33.543713	12.55	3385	66	541.	0.0043	98	1	N
J06107+2556	92.693016	25.933996	11.53	4344	109	1587.	0.0060	98	0	N
J06409+6353	100.236435	63.890373	11.27	820	18	130.	0.0046	56	17	N
J06461+3233	101.531082	32.554173	11.86	1245	19	1636.	0.0037	64	7	N
J06486+5317	102.160187	53.291550	12.22	281	10	773.	0.0103	0	40	N
J06563+5458	104.097519	54.974411	12.53	472	12	39.	0.0047	30	24	N
J07039+5242	105.982224	52.701839	13.73	2551	77	565.	0.0045	84	1	N
J07078+6449	106.960747	64.822601	12.64	212	9	1518.	0.0047	0	41	N
J07136+5037	108.407845	50.628231	12.30	9605	133	1499.	0.0035	100	0	N
J07140+5043	108.518837	50.725895	11.51	3135	75	1228.	0.0051	94	0	N
J07232+4605	110.812096	46.087440	10.56	5962	146	1478.	0.0059	99	0	N
J07493+8458	117.331467	84.977249	13.04	5263	145	998.	0.0060	96	0	N
J07493+8448	117.346375	84.808586	12.84	4536	130	640.	0.0042	90	0	N
J08255+5824	126.382660	58.414440	12.49	3412	78	740.	0.0041	99	0	N
J08417+2318	130.428680	23.312967	13.69	1107	28	1482.	0.0077	7	18	N
J08474+2935	131.865082	29.585402	12.19	2873	64	490.	0.0047	80	0	N
J08512+2538	132.803223	25.649866	12.50	3678	85	740.	0.0045	90	0	N
J09018+3251	135.454788	32.851627	13.43	5429	170	1529.	0.0050	100	0	N
J09203+3221	140.088867	32.363087	13.48	1899	45	409.	0.0048	56	0	N
J09473+2618	146.843369	26.303535	10.91	1220	47	1495.	0.0057	65	9	N
J09569+3202	149.243500	32.038227	13.45	303	7	1479.	0.0072	0	26	N
J10094+5117	152.374863	51.288826	13.92	2496	65	556.	0.0044	84	0	N
J10205+4653	155.145126	46.893467	13.12	1569	44	851.	0.0040	78	0	N
J10273+7959	156.847305	79.997543	12.29	4669	147	1068.	0.0047	92	0	N
J11054+4331	166.345900	43.530600	0.00	4802	118	1063.	0.0031	99	0	N
J11190+4900	169.767258	49.001083	12.50	4371	98	1638.	0.0043	100	0	N
J12135+3112	183.396667	31.214161	13.73	1859	56	1191.	0.0073	62	9	N
J12505+4022E	192.637222	40.370083	11.56	3072	64	436.	0.0043	73	0	N
J12513+2206	192.849701	22.104149	13.20	3478	76	1594.	0.0050	89	0	N
J13165+2752	199.136841	27.874937	13.70	1462	42	514.	0.0049	42	5	N
J13195+3506W	199.889967	35.110157	0.00	4811	50	794.	0.0052	88	0	N
J13196+3320	199.917287	33.346607	0.00	968	23	71.	0.0072	12	28	N
J13201+8512	200.044083	85.214577	12.18	4758	90	577.	0.0045	88	0	N
J13255+2738	201.398605	27.635530	12.80	927	33	477.	0.0044	65	12	N
J13342+3751	203.561371	37.858685	12.30	2819	63	421.	0.0036	86	0	N
J13348+2011	203.705627	20.194075	14.25	2914	40	776.	0.0067	43	14	N
J13394+4611	204.850438	46.186520	0.00	2037	89	1161.	0.0042	80	1	N
J13445+2457	206.140259	24.951550	12.04	659	18	372.	0.0043	22	20	N
J14023+1341	210.581709	13.689717	0.00	802	19	36.	0.0059	23	30	N
J14279+3109	216.984970	31.154264	13.17	1919	68	858.	0.0046	92	0	N
J14294+1531	217.373744	15.532639	0.00	1130	34	58.	0.0042	35	24	N
J15043+2928	226.092743	29.478508	12.94	631	22	117.	0.0046	33	25	N
J15513+2931	237.840805	29.518476	13.33	211	7	25.	0.0055	1	35	N

Table A1: Continued.

Name	RA (deg)	Dec (deg)	V (mag)	N points	N nights	ΔHJD (days)	σ_r (mag)	Φ_{det} (%)	$\Phi_{det,h}$ (%)	Rotator Yes/No
J16018+3027	240.469162	30.459713	13.69	2748	106	1423.	0.0046	92	0	N
J16090+5256	242.262906	52.943874	0.00	176	6	252.	0.0050	4	39	N
J16255+3218	246.386826	32.308159	12.54	2364	99	884.	0.0041	94	0	N
J16395+5034	249.876038	50.567677	11.88	4962	113	1553.	0.0055	89	0	N
J16529+4005	253.229172	40.085670	13.83	3822	111	1452.	0.0049	98	0	N
J16590+2938	254.757202	29.634945	11.82	424	27	361.	0.0039	15	27	N
J17198+4142	259.969448	41.714188	0.00	3639	105	1119.	0.0052	81	0	N
J17355+6140	263.893583	61.681671	0.00	2284	72	499.	0.0043	81	0	N
J17395+2746	264.884308	27.776867	13.19	1913	76	807.	0.0053	61	11	N
GJ694.2	266.389753	46.855396	0.00	2075	61	599.	0.0048	60	5	N
GJ694.2	266.389753	46.855396	0.00	1043	34	337.	0.0045	36	21	N
J17578+4635	269.462341	46.588562	11.79	960	26	1751.	0.0082	4	27	N
J17589+8042	269.736176	80.712204	0.00	539	16	73.	0.0045	8	25	N
J18250+2438	276.269957	24.634562	0.00	3428	109	1137.	0.0051	90	0	N
J18396+1623	279.909973	16.387083	12.75	591	22	40.	0.0055	6	30	N
J18518+1634	282.963287	16.583347	10.16	2475	97	1423.	0.0067	79	5	N
J19284+2854	292.106354	28.902832	11.04	988	40	402.	0.0042	43	9	N
J19395+7152	294.887024	71.872047	10.94	2928	106	1266.	0.0051	98	0	N
J19457+2707	296.439545	27.125463	12.25	1637	35	42.	0.0071	31	26	N
J19502+3147	297.566437	31.783455	12.93	1404	30	39.	0.0055	37	25	N
J20129+3416S	303.228790	34.277687	11.12	1206	47	805.	0.0047	86	0	N
J20138+1323	303.465820	13.388809	11.30	840	33	122.	0.0044	28	27	N
J20260+5834	306.522034	58.572926	15.08	1094	25	35.	0.0042	38	27	N
J20269+2730	306.734558	27.516272	12.13	3327	102	1477.	0.0056	97	0	N
J20305+6526	307.633655	65.449623	0.00	898	21	98.	0.0098	9	34	N
J20315+5557	307.886810	55.963417	10.12	769	41	105.	0.0059	34	25	N
J20336+6145	308.417969	61.753792	12.66	1223	28	70.	0.0063	36	22	N
J20450+4429	311.266998	44.499035	10.79	1458	36	1779.	0.0077	34	18	N
J21275+3401	321.887360	34.024639	11.06	3835	115	1167.	0.0054	93	0	N
J21380+2743	324.501526	27.723755	9.83	1211	38	740.	0.0117	18	32	N
J21399+2736	324.976532	27.612093	11.62	1745	31	38.	0.0067	34	29	N
J21448+4417	326.224976	44.285767	11.56	5649	149	1127.	0.0036	100	0	N
J21482+2755	327.063629	27.928354	12.03	2343	65	518.	0.0054	71	1	N
J21521+2725	328.049103	27.416780	14.36	236	10	1763.	0.0050	0	33	N
J21539+4146	328.495789	41.779076	10.30	746	29	1802.	0.0065	12	15	N
J21584+7535	329.602020	75.589058	10.56	316	10	71.	0.0047	32	28	N
J22018+1628	330.454315	16.467430	10.65	1127	30	493.	0.0098	7	24	N
J22033+6729	330.838501	67.499947	13.52	2660	61	103.	0.0051	57	11	N
J22112+4100	332.820679	41.015198	11.11	6168	164	1600.	0.0059	100	0	N
J22133+7534	333.338287	75.583298	12.86	4335	124	856.	0.0037	96	0	N
J22228+2801	335.711945	28.029846	14.09	1306	41	1540.	0.0047	64	13	N
J22252+5924	336.321014	59.413834	13.04	2177	41	1593.	0.0066	44	7	N
J22355+3712	338.896027	37.203663	11.93	4033	125	1209.	0.0045	100	0	N
J22415+1849	340.395752	18.824299	10.82	1839	43	136.	0.0086	34	17	N
J22440+4030	341.019226	40.500057	11.57	2369	88	1221.	0.0048	99	0	N
J22441+4030	341.026093	40.500107	11.55	4441	117	1190.	0.0049	97	0	N
J22507+2836	342.689667	28.602335	12.68	840	31	392.	0.0049	66	13	N
J22535+8130	343.396942	81.512573	11.96	4348	108	734.	0.0043	90	0	N
J22554+6214	343.871857	62.239120	10.61	5462	107	782.	0.0081	96	0	N
J22559+1748	343.999390	17.811062	10.62	5753	161	1600.	0.0049	99	0	N
J23045+6645	346.125763	66.764397	9.86	2613	70	1640.	0.0073	81	5	N
J23204+7442	350.101837	74.702332	13.72	623	17	67.	0.0046	28	20	N
J23354+3003	353.851227	30.062487	13.35	363	15	1542.	0.0055	2	28	N
J23438+3235	355.971252	32.594120	12.39	1448	34	493.	0.0060	26	21	N
J23451+3003	356.286163	30.055134	14.40	647	13	1055.	0.0053	25	29	N
J23462+2826	356.558624	28.434376	13.20	3271	85	667.	0.0056	85	0	N

Table A2: Continued.

Name	B-V (mag)	Plx (mas)	T_{eff} (K)	Mass (M_{\odot})	Radius (R_{\odot})	V_R (km/s)	V_{ϕ} (km/s)	V_Z (km/s)	Period (Days)	Amp (mag)	Fap
J13517+3142	1.392	14.4020 ± 0.0330	4081 ⁺¹⁶⁹ ₋₂₃₄	0.545 ± 0.046	0.504 ± 0.070	—	—	—	40.5789	0.0034	0.0003
J13580+3141	1.383	13.5797 ± 0.0282	4068 ⁺¹⁰² ₋₉₅	0.565 ± 0.063	0.504 ± 0.134	13.6	229.9	-2.6	12.9731	0.0053	0.0019
J14257+2337W	1.472	61.1783 ± 0.0542	3965 ⁺¹³³ ₋₅₄	0.515 ± 0.061	0.454 ± 0.150	-114.6	223.3	-13.7	17.3665	0.0045	0.0014
J14294+1531	1.500	70.1774 ± 0.0505	—	—	—	85.7	265.6	59.7	12.5735	0.0046	0.0005
J15297+4252	1.698	50.4856 ± 0.4258	4288 ⁺⁵²⁴ ₋₁₀₁₃	0.230 ± 0.050	0.237 ± 0.035	-83.8	247.8	-2.7	89.0242	0.0027	0.0004
J15336+4615	1.622	43.2181 ± 0.0374	4076 ⁺¹⁵⁴ ₋₅₂₂	0.295 ± 0.053	0.281 ± 0.036	10.4	241.7	-14.1	189.5937	0.0058	0.0000
J16008+4019	1.553	47.3115 ± 0.0289	3859 ⁺¹⁵⁴ ₋₂₃₀	0.315 ± 0.049	0.291 ± 0.034	-15.1	186.2	-6.7	191.8277	0.0042	0.0001
J16072+2650	1.664	44.3889 ± 0.0355	3819 ⁺¹⁷⁷ ₋₂₃₈	0.335 ± 0.063	0.310 ± 0.048	-62.0	240.2	-29.5	179.4527	0.0036	0.0007
J16254+5418	1.718	154.4710 ± 0.0273	3763 ⁺¹⁹⁶ ₋₃₃	0.380 ± 0.067	0.361 ± 0.097	-20.6	243.0	-9.6	87.9696	0.0053	0.0000
J16259+8324	1.625	34.5643 ± 0.0268	3982 ⁺¹⁹⁶ ₋₁₃₆	0.500 ± 0.069	0.446 ± 0.100	-26.4	248.4	0.4	16.9066	0.0039	0.0000
J16408+3619	1.513	46.5739 ± 0.0391	3928 ⁺⁵³ ₋₂₂₃	0.460 ± 0.062	0.423 ± 0.066	35.2	198.5	-30.1	32.5186	0.0029	0.0015
J16420+1916	1.438	32.3055 ± 0.0478	3691 ⁺¹⁴¹ ₋₉₂	0.355 ± 0.064	0.330 ± 0.075	—	—	—	30.9335	0.0035	0.0053
J17104+2758W	1.616	42.7700 ± 0.0310	3735 ⁺²⁶⁵ ₋₄₂₄	0.310 ± 0.087	0.300 ± 0.091	-9.6	228.6	-8.2	27.6892	0.0030	0.0012
J17158+1900	1.520	73.1060 ± 0.0336	3731 ⁺¹²⁴ ₋₁₀₁	0.300 ± 0.093	0.289 ± 0.118	3.1	228.5	5.5	14.5440	0.0040	0.0078
J17160+1103	1.507	55.0799 ± 0.0497	3889 ⁺¹¹⁹ ₋₁₆₂	0.460 ± 0.067	0.414 ± 0.093	4.1	196.9	-14.0	32.9925	0.0040	0.0002
J17166+0803	1.557	66.1437 ± 0.0402	3815 ⁺⁵⁹ ₋₁₂₈	0.415 ± 0.054	0.373 ± 0.052	11.1	217.0	9.1	45.6910	0.0025	0.0031
J17312+8205	1.818	77.7089 ± 0.0425	3353 ⁺¹²⁹ ₋₅₉	0.195 ± 0.054	0.228 ± 0.041	36.1	272.3	43.3	99.5127	0.0035	0.0001
J17378+1835	1.426	122.5609 ± 0.0346	3990 ⁺¹⁰³ ₋₉₆	0.450 ± 0.045	0.391 ± 0.036	21.1	280.7	-13.5	34.6720	0.0028	0.0013
J17395+2745	1.436	35.9730 ± 0.0240	3902 ⁺¹⁵² ₋₁₀₂	0.475 ± 0.049	0.428 ± 0.103	-44.1	246.5	6.7	26.1763	0.0029	0.0011
J17589+8042	1.442	31.2262 ± 0.9523	3936 ⁺⁶³ ₋₁₃₈	0.425 ± 0.046	0.371 ± 0.036	—	—	—	138.9877	0.0056	0.0000
J18234+2810	1.761	67.5255 ± 0.0617	3560 ⁺³³ ₋₂₇₅	0.240 ± 0.078	0.247 ± 0.088	-28.3	244.0	10.5	7.8355	0.0027	0.0019
J18353+4544	1.373	64.2488 ± 0.0250	4060 ⁺⁵²³ ₋₉₆	0.495 ± 0.066	0.438 ± 0.064	27.2	234.9	-26.3	33.6225	0.0027	0.0001
J18563+5429W	1.543	23.6502 ± 0.0712	3911 ⁺⁹⁴ ₋₁₇₆	0.475 ± 0.070	0.420 ± 0.180	-74.0	235.2	-25.3	82.3117	0.0034	0.0012
J18580+0554	1.411	90.0477 ± 0.0490	3920 ⁺²⁰⁷ ₋₁₇₇	0.470 ± 0.069	0.450 ± 0.091	-59.6	203.9	-12.1	35.6422	0.0063	0.0000
J18596+0759	1.380	35.4261 ± 0.0408	4052 ⁺¹⁷⁷ ₋₁₂₄	0.550 ± 0.055	0.497 ± 0.091	50.0	192.2	-49.5	43.4095	0.0036	0.0022
J19242+7943	1.422	27.8400 ± 0.0257	4000 ⁺¹⁴⁷ ₋₁₄₁	0.515 ± 0.061	0.474 ± 0.090	-6.4	236.5	-8.8	15.9090	0.0027	0.0003
J19540+3233	1.496	21.6392 ± 0.0548	3911 ⁺¹¹⁶ ₋₁₉₅	0.475 ± 0.070	0.427 ± 0.127	55.0	210.8	-9.1	22.1328	0.0050	0.0024
J20586+3416	1.337	39.7652 ± 0.0448	4065 ⁺¹⁰² ₋₁₀₂	0.515 ± 0.048	0.455 ± 0.050	-4.4	253.9	-31.0	40.3242	0.0056	0.0001
J21012+3314	1.799	45.9752 ± 0.5444	3704 ⁺²⁷⁸ ₋₁₈₄	0.285 ± 0.089	0.276 ± 0.124	7.4	206.9	-22.4	29.5842	0.0048	0.0001
J21109+2925	1.375	—	—	—	—	23.5	238.7	-11.3	39.2636	0.0032	0.0002
J21129+3107E	1.636	24.6435 ± 0.0349	3957 ⁺¹³⁹ ₋₁₅₇	0.480 ± 0.063	0.424 ± 0.222	-29.1	244.2	-6.9	20.8400	0.0028	0.0001
J21152+2547	1.485	37.4114 ± 0.0533	3579 ⁺¹⁸⁰ ₋₈₈	0.295 ± 0.060	0.291 ± 0.111	-12.8	197.2	-15.8	48.1739	0.0044	0.0000
J21179+3404	1.266	24.1211 ± 0.3098	—	—	—	—	—	—	13.8088	0.0028	0.0002
J21185+3014	1.181	26.7573 ± 0.0428	3866 ⁺¹⁵⁹ ₋₉₁	0.325 ± 0.030	0.303 ± 0.021	-2.6	223.2	2.7	8.0086	0.0327	0.0000
J21185+3014	1.181	26.7573 ± 0.0428	3866 ⁺¹⁵⁹ ₋₉₁	0.325 ± 0.030	0.303 ± 0.021	-2.6	223.2	2.7	8.0603	0.0119	0.0000
J21366+3927E	1.446	48.2934 ± 0.1828	3951 ⁺²⁴⁸ ₋₃₈₀	0.455 ± 0.086	0.437 ± 0.129	-38.1	245.4	10.3	36.6415	0.0039	0.0001
J21487+4019	1.571	1.5880 ± 0.0360	4072 ⁺⁶⁴ ₋₃₃	0.540 ± 0.029	0.469 ± 0.026	—	—	—	77.4330	0.0031	0.0007
J22006+2715	1.296	28.1182 ± 0.0287	3986 ⁺¹⁸⁵ ₋₃₇₈	0.510 ± 0.067	0.474 ± 0.079	-3.6	242.4	-1.9	0.5228	0.0125	0.0000
J22107+0754	1.461	—	—	—	—	—	—	—	14.8962	0.0061	0.0000
J22129+5504N	0.889	18.1300 ± 0.2090	4084 ⁺¹⁰⁵ ₋₆₉	0.655 ± 0.047	0.782 ± 0.097	—	—	—	4.8678	0.0043	0.0007
J22154+6613	1.663	55.9143 ± 0.0517	3860 ⁺⁹⁹ ₋₁₈₅	0.380 ± 0.056	0.333 ± 0.043	0.7	252.6	23.8	63.1108	0.0149	0.0002
J22385+8309	1.513	17.1745 ± 0.0213	4201 ⁺¹⁷⁵ ₋₂₄₆	0.590 ± 0.070	0.535 ± 0.104	49.7	194.6	11.0	29.3248	0.0031	0.0007
J22562+5919	1.392	21.6894 ± 0.0301	4104 ⁺¹⁶⁹ ₋₇₅	0.580 ± 0.068	0.530 ± 0.145	11.0	200.4	17.9	13.9597	0.0051	0.0013
J23182+7934	1.551	28.9440 ± 0.0360	3832 ⁺¹⁴² ₋₃₉₉	0.335 ± 0.049	0.307 ± 0.039	—	—	—	55.4611	0.0035	0.0006
J23313+5944	1.455	2.6360 ± 0.0240	4088 ⁺¹¹⁴ ₋₃₉	0.545 ± 0.031	0.473 ± 0.029	35.0	219.6	29.5	6.1388	0.0038	0.0017
J23428+3049	1.876	77.9876 ± 0.1206	3657 ⁺³⁶ ₋₂₁₀	0.270 ± 0.036	0.263 ± 0.026	-40.0	240.4	2.0	11.2172	0.0032	0.0000
J23513+2344	1.598	39.1767 ± 0.0811	3639 ⁺³⁹¹ ₋₃₃₅	0.240 ± 0.054	0.245 ± 0.038	11.2	225.7	-5.5	3.2080	0.0184	0.0000
J23515+3127	1.417	23.2183 ± 0.0524	4038 ⁺²⁶⁰ ₋₃₀₉	0.335 ± 0.058	0.302 ± 0.040	-3.7	218.5	-5.5	1.8036	0.0028	0.0015

This paper has been typeset from a \TeX/L\AA\TeX file prepared by the author.